

BACHELORARBEIT / BACHELOR'S THESIS

Titel der Bachelorarbeit / Title of the Bachelor's Thesis

"Microwave Spectroscopy of Propagating Spin Waves in Macroscale YIG Films"

verfasst von / submitted by Wolfgang Czingraber

angestrebter akademischer Grad / in partial fulfilment of the requirements for the degree of

Bachelor of Science (BSc)

Wien, 2025 / Vienna, 2025

Studienkennzahl It. Studienblatt / degree programme code as it appears on the student record sheet:

UA 033 676

Disserationsgebiert It. Studienblatt / field of study as it appears on the student record sheet:

Bachelor Physics

Betreut von / Supervisor: Mitbetreut von / Co-Supervisor: Univ.-Prof. Dr. habil. Andrii Chumak Dr. Khrystyna Levchenko

Acknowledgements

Above all, I am profoundly grateful to Dr. Khrystyna Levchenko for her constant support and feedback throughout the creation of this thesis. Her guidance and advice have allowed me to gain the necessary skills, experience, and knowledge—not only for conducting the experiments, presentations, and scientific writing, but also for my future work in scientific environments. I also want to thank Prof. Andrii Chumak for supervising my thesis and giving me the opportunity to work in the research field of "Nanomagnetism and Magnonics". He helped to enhance my understanding of magnetism and supported me at every step of the thesis.

In addition, I would like to thank Dr. Franz Vilsmeier, Rostyslav Serha, and David Schmoll for their helpful input. I especially want to mention Kristýna Davídková for familiarising me with the topic of propagating spin wave spectroscopy and for introducing me to the experimental setup. She also gave me the opportunity to gain experience with 3D modelling software and to contribute to the current experimental setup.

I want to express my gratitude to my friends, particularly Nicolas and Nina, who helped and motivated me throughout my studies. Last but not least, I wish to thank my parents, Sabine and Thomas, and my brothers, Stefan and Roman, for their unlimited support, encouragement, and open arms.

Abstract

The collective excitations of spins in magnetic materials, called spin waves, show great potential for future technologies, most notably in high-frequency applications [1,2]. Among other factors, the geometry of the waveguide and the relative orientation of an externally applied magnetic field are crucial in determining the characteristics of the propagating spin waves [3].

This thesis aims to analyse and demonstrate the influence of varying thicknesses of macroscopically thick YIG/GGG films on signal transmission, and to contribute to the experimental setup by designing an improved Hall probe holder for future use. The new holder design seeks to allow better access, finer adjustment, and reduced interference with the sample holder. Three different films with thicknesses of $4.1\mu m$, $7.78\mu m$, and $22.83\mu m$ are measured under an in-plane bias field in a linear regime. Both the Damon–Eshbach (DE)/magnetostatic surface spin waves (MSSW) and backward volume magnetostatic spin waves (BVMSW) are investigated by means of a propagating spin-wave spectroscopy (PSWS) technique using a vector network analyser (VNA) and microstrip excitation antennas, in a wide frequency range of 1-25 GHz and external fields up to 800 mT.

The experimental results show strong agreement with the theoretical analysis, with the most notable observation being that DE/MSSW modes and thicker samples exhibit the lowest losses. The strong correlation to theoretical calculations based on dipole approximations indicates that exchange interactions contribute insignificantly, and that dipole interactions dominate at the macroscale. Overall, the findings highlight the potential and versatility of spin-wave signals, allowing for significant adaptability in future devices.

Zusammenfassung

Spinwellen, kollektive Anregungen von Spins in magnetischen Materialien, zeigen großes Potenzial für zukünftige Technologien – insbesondere im Bereich von Hochfrequenzanwendungen [1, 2]. Neben anderen Faktoren spielt die Geometrie des Wellenleiters sowie die relative Ausrichtung des externen Magnetfelds eine entscheidende Rolle für die Eigenschaften propagierender Spinwellen [3].

Ziel dieser Arbeit ist es, den Einfluss der Probendicke von makroskopisch dünnen YIG/GGG-Schichten auf die Signalübertragung zu untersuchen und einen Beitrag zum experimentellen Aufbau zu leisten, indem eine verbesserte Halterung für die Hallsonde entworfen wird. Das neue Design verspricht besseren Zugang, feinere Justierung und geringere Störeinflüsse auf die Probenhalterung.

Drei Filme mit Dicken von $4.1\mu m$, $7.78\mu m$ und $22.83\mu m$ werden in einem Magnetfeld vermessen, das in der Filmebene orientiert ist. Sowohl Damon-Eshbach-(DE) bzw. magnetostatische Oberflächen-Spinwellen (MSSW) als auch rückwärtige volumenhafte magnetostatische Spinwellen (BVMSW) werden mithilfe eines Vektornetzwerkanalysators (VNA) und Mikrostreifenleitungen, die als Anregungsantennen dienen, im Frequenzbereich von $1-25 {\rm GHz}$ untersucht. Das externe Magnetfeld wird dabei im Bereich von $0-800 {\rm mT}$ variiert.

Die experimentellen Daten zeigen eine starke Übereinstimmung mit der theoretischen Analyse. Besonders bemerkenswert ist die Beobachtung, dass dickere Filme und DE/MSSW-Moden die geringsten Verluste aufweisen. Die starke Korrelation mit den theoretischen Berechnungen unter Berücksichtigung der Dipolwechselwirkungen deutet darauf hin, dass Austauschwechselwirkungen in makroskopischen Dimensionen keine signifikanten Auswirkungen haben und stattdessen die Dipolwechselwirkungen dominieren. Insgesamt verdeutlichen die Ergebnisse das Potenzial und die Vielseitigkeit von Spinwellensignalen, was einen großen Spielraum für Anpassungen in zukünftigen Technologien eröffnet.

Contents

Acknowledgements Abstract				
1	Intro	oduction	8	
2	The	oretical Background	10	
	2.1	The basics of magnetism	10	
		2.1.1 Magnetic fields in magnetic materials	11	
		2.1.2 Landau-Lifshitz-Gilbert equation	14	
		2.1.3 Magnetic properties of materials	15	
	2.2	Spin Dynamics	18	
		2.2.1 Ferromagnetic resonance	18	
		2.2.2 Spin waves of thin films	19	
		2.2.3 Propagating Spin-Wave Spectroscopy	22	
	2.3	Yttrium Iron Garnet (YIG)	25	
3	Setu	ıp upgrade	27	
4	Met	hodology	29	
	4.1	Experimental setup	29	
	4.2	Measurements	30	
	4.3	Analysis	31	
5	Res	ults	34	
	5.1	Overview: FMR, dispersion relation	34	
	5.2	FFT: delay time, group velocity and characteristics	39	
6	Disc	cussion	49	
	6.1	Raw data	49	
	6.2	FMR	49	
	6.3	Dispersion relation	50	

	6.4	Time gating	51	
	6.5	Group velocity and delay time	51	
	6.6	Insertion loss, dynamic range, bandwidth	52	
7	Conclusion and Outlook			
Re	References			
Αį	Appendix			

1 Introduction

A spin wave (SW) represents a collective excitation of a spin system in a magnetically ordered medium [4]. The quanta of these excitations are called magnons [5]. Magnonics, which is often grouped under the broader umbrella of magnon spintronics, investigates information transport and processing through SWs as an alternative to, or in conjunction with, charge currents [3].

Magnons themselves are charge-neutral quasiparticles, unlike electron currents in conventional electronics, which allows them to propagate without energy dissipation, i.e., without Joule heating. Owing to their inherent wave nature, information in SWs can be encoded simultaneously in amplitude, phase, and frequency. Although research on SW phenomena is less than a century old, rapid development of the field has given rise to a variety of advanced device concepts. These developments offer a promising alternative to conventional RF and CMOS technologies, and pave the way for cutting-edge fields such as magnonic neuromorphic and quantum computing [1,6].

Due to its excellent insulating and magnetic properties, Yttrium Iron Garnet (YIG) especial grown on a Gadolinium Gallium Garnet (GGG) substrate, is the exemplary material used in both fundamental and applied magnonics [6]. Among the various experimental techniques available, PSWS offers a convenient, all-electrical method for both the excitation and detection of SWs [4,7].

In this thesis, the PSWS methodology is used to investigate how the SW dynamics in macroscale-large, micrometer-thick YIG films, where the dipolar interactions dominate, depend on film thickness [8]. In particular, the transmission spectra are measured for the BVMSW and DE (MSSW) modes, and the results are compared with the analytical calculations. This includes extraction and analysis, such as FMR, dispersion relations, delay time, and excitation characteristics.

Furthermore, this thesis covers a redesign of the Hall sensor holder used for magnetic field measurements. The new construction allows for easier access and finer adjustments, leading to improved accuracy of the magnetic field measurements.

The thesis is organised as follows: after the Introduction chapter, the relevant the-

oretical background of magnetism, spin dynamics, as well as the principles of the experimental devices, is explained in Chapter 2. Chapter 3 describes the improvements to the Hall probe holder design, while Chapter 4 explains the experimental setup used for the measurements. In Chapter 5, the results are presented, which are then discussed in Chapter 6. In the end, Chapter 7 gives the conclusion and the outlook of the thesis.

2 Theoretical Background

This chapter describes the fundamental principles of magnetism and the methodology required for the excitation, measurement, and analysis of spin waves.

2.1 The basics of magnetism

The magnetic moment of an atom arises from its electrons. An electron orbiting the nucleus can be regarded as a current loop, contributing an orbital magnetic moment. Additionally, the electron's intrinsic spin behaves similarly, generating a spin magnetic moment. These contributions, denoted as μ_L and μ_S respectively, are given by:

$$\mu_{\mathbf{L}} = -\frac{e}{2m_{\mathbf{e}}}\mathbf{L}, \quad \mu_{\mathbf{S}} = -g\frac{e}{2m_{\mathbf{e}}}\mathbf{S} \approx -\frac{e}{m_{\mathbf{e}}}\mathbf{S},$$
 (1)

where e is the elementary charge, and ${\bf L}$ and ${\bf S}$ are the vector sums of the orbital and spin angular momenta of all electrons in the atom; $m_{\rm e}$ is the mass of the electron, and g is the g-factor, which is experimentally determined to be ≈ 2.003 for a free electron. The term $-\frac{ge}{2m_{\rm e}}=\gamma$ is called the $\it gyromagnetic ratio$, which is the proportionality factor between the magnetic moment and the angular momentum.

To calculate the total magnetic moment μ of an atom, the sum of the orbital and spin magnetic moments must be considered:

$$\mu = \mu_S + \mu_L = -g_{atom} \frac{e}{2m_e} J \approx -\frac{e}{2m_e} (2S + L),$$
 (2)

where J is the total angular momentum vector [5].

An important quantity in magnetism is the magnetisation M, which is defined as the density of magnetic moments μ per unit volume V. The magnetisation is therefore expressed as:

$$M = \frac{\sum_{\Delta V} \mu}{\Delta V},\tag{3}$$

where ΔV is the macroscopic volume [2]. The highest magnetisation a given material can reach is called the *saturation magnetisation*, $M_{\rm S}$, and occurs when all magnetic moments are aligned within the material [5]. The *magnetic field H* is

given by the relation:

$$H = \chi M, \tag{4}$$

where χ is the *magnetic susceptibility* - a characteristic of a material, which describes its magnetic response to an applied field [5, 9].

2.1.1 Magnetic fields in magnetic materials

Another important quantity in electromagnetism is the *magnetic flux density* B, which describes the response of a medium to a magnetic field H. The relationship between the two fields B_0 and H_0 in a vacuum is given by:

$$\boldsymbol{B}_0 = \mu_0 \boldsymbol{H}_0, \tag{5}$$

where $\mu_0 = 4\pi \cdot 10^{-7} \frac{\mathrm{Vs}}{\mathrm{Am}}$ is the vacuum magnetic permeability.

For a magnetic material, the magnetisation M inside the sample produces a demagnetising field $H_{\rm d}$ that opposes the applied field $H_{\rm ext}$, resulting in the following expression:

$$\boldsymbol{H}_{\text{int}} = \boldsymbol{H}_{\text{ext}} + \boldsymbol{H}_{\text{d}} = \boldsymbol{H}_{\text{ext}} - N_{\text{d}} \boldsymbol{M}, \tag{6}$$

Here, $N_{\rm d}$ is the demagnetisation factor. In vacuum or in weak magnetic materials, where $|{m M}| \ll |{m H}_{\rm ext}|$, the equation reduces to ${m H}_{\rm int} = {m H}_{\rm ext}$ [5].

The flux density B inside materials follows from Maxwell's equations [4]:

$$\boldsymbol{B} = \mu_0 (\boldsymbol{H}_{\text{int}} + \boldsymbol{M}). \tag{7}$$

The dynamics of magnetisation within a material are governed by the total energy of the system. In equilibrium, the orientation of the magnetic moments in an external magnetic field minimises the total internal energy of the material, $E_{\rm total}$, accounting for contributions from the external field and internal magnetic interactions, given by:

$$E_{\text{total}} = E_{\text{ex}} + E_{\text{Z}} + E_{\text{d}} + E_{\text{ani}} + ...,$$
 (8)

where the energy terms $E_{\rm i}$ represent the exchange energy, Zeeman energy, de-

magnetisation energy, and magnetocrystalline anisotropy energy, respectively. Each energy term corresponds to a contribution to the effective magnetic field $\boldsymbol{H}_{\mathrm{eff}}$ which is calculated as the sum of the corresponding field components:

$$\boldsymbol{H}_{\text{eff}} = -\frac{1}{\mu_0} \nabla_{\boldsymbol{M}}(E_{\text{total}}) = \boldsymbol{H}_{\text{d}} + \boldsymbol{H}_{\text{ex}} + \boldsymbol{H}_{\text{ext}} + \boldsymbol{H}_{\text{a}} + ...,$$
(9)

where $H_{\rm ex}$ and $H_{\rm a}$ denote the exchange field and anisotropy field, respectively. A common method used to compute the effective magnetic field $H_{\rm eff}$ is micromagnetics [4, 6, 10, 11].

Dipole energy and demagnetisation field

When a material is magnetised, the arrangement of its magnetic moments generates a demagnetising field $H_{\rm d}$ through weak but long-range *dipolar interactions*. This field is oriented in the opposite direction to the external magnetic field:

$$\boldsymbol{H}_{\mathrm{d}} = -N_{\mathrm{d}} \cdot \boldsymbol{M},\tag{10}$$

where $N_{\rm d}$ is the demagnetising tensor and M is the magnetisation. For a thin film that is oriented orthogonally to the z-axis, the demagnetising tensor takes the form [5]:

$$N_{\rm d} = \begin{pmatrix} 0 & 0 & 0 \\ 0 & 0 & 0 \\ 0 & 0 & 1 \end{pmatrix} \tag{11}$$

The dipolar energy $E_{\rm dipole}$, also known as magnetostatic energy, arises from the long-range magnetic interactions between magnetic moments within the material and is expressed as:

$$E_{\text{dipole}} = -\frac{\mu_0}{2} \int_{V} \boldsymbol{M} \cdot \boldsymbol{H}_{\text{d}} dV, \tag{12}$$

where V is the volume of the sample. The dipole energy depends strongly on the geometry of the magnetic material. The minimum dipole energy state is reached when the magnetic moments align antiparallel, thereby minimising the stray field [5, 11]. The exact configuration of the magnetic moments results from the combined influences of the exchange energies, anisotropy energies, and dipole energy [5].

Exchange energy

The exchange energy originates from the quantum mechanical effects, resulting in a strong but short-range *exchange interaction* between neighbouring spins S_i and S_j . The corresponding exchange energy $E_{\rm ex}$ is given by:

$$E_{\rm ex} = -2\sum_{\rm i,j} J_{\rm ij} \boldsymbol{S}_{\rm i} \cdot \boldsymbol{S}_{\rm j}, \tag{13}$$

where J_{ij} is the exchange integral, and S_i, S_j are the spin operators. In *ferromagnetic materials*, $J_{ij} > 0$, which favours parallel alignment of neighbouring spins to minimise $E_{\rm ex}$. In contrast, when $J_{ij} < 0$, antiparallel alignment is favoured, typically resulting in antiferromagnetic ordering [5]. The resulting exchange field $H_{\rm ex}$ can be derived from the exchange energy $E_{\rm ex}$ and is given by:

$$\boldsymbol{H}_{\text{ex}} = \frac{2ZJ}{\mu_0 N g^2 \mu_{\text{B}}^2} [\boldsymbol{M} + \frac{R_{\text{n}}^2}{6} \nabla^2 \boldsymbol{M}],$$
 (14)

where Z is the number of nearest neighbours, $R_{\rm n}$ the nearest-neighbour distance, $N=\frac{-g\mu_{\rm B}S}{M}$ is the density of moments, $\mu_{\rm B}$ the Bohr magneton, and g the g-factor [4].

A characteristic quantity for the transition between dipole energy and exchange energy is the exchange length $l_{\rm ex}$. This describes the distance at which the exchange energy starts to dominate the dipole energy and is given by:

$$l_{\rm ex} = \sqrt{\frac{A_{\rm ex}}{\mu_0 M_{\rm S}^2}},\tag{15}$$

where $A_{\rm ex}$ is the material-dependent exchange constant [5, 9, 11].

Anisotropy energy

The *anisotropy energy* arises due to spin-orbit coupling interactions, resulting in non-spherical symmetry. The energy therefore depends on the relative orientation of the orbitals with respect to the ions in a crystal. In materials with uniaxial anisotropy, there exists an axis along which the energy is either minimised or maximised. In the case of minimisation, this axis is referred to as the "easy" axis. If the energy is maximised, the axis is known as the "hard" axis. If θ is the angle

between the easy axis and the magnetisation M, then the anisotropy energy $E_{\rm a}$ is given by:

$$E_{\rm a} = \int_{V} K_{\rm u} \sin^2 \theta dV \tag{16}$$

For a cubic structure, the magnetocrystalline anisotropy energy $E_{\rm a}$ can be expressed by the lowest-order expansion of the cubic anisotropy energy:

$$E_{\rm a} = K_{\rm 1c}(\alpha_1^2 \alpha_2^2 + \alpha_2^2 \alpha_3^2 + \alpha_3^2 \alpha_1^2) + K_{\rm 2c}(\alpha_1^2 \alpha_2^2 \alpha_3^2), \tag{17}$$

where $K_{\rm ic}$ are the anisotropy coefficients, and the components of the normalised magnetisation vector M are represented by the direction cosines α_i of each axis, which satisfy the relation $\alpha_1^2 + \alpha_2^2 + \alpha_3^2 = 1$ [4,9].

Zeeman energy

The potential energy created by the interaction between a uniform external field H_{ext} and the magnetic dipole moment m is called the Zeeman energy E_{Z} , and is expressed as:

$$E_{\rm Z} = -\mu_0 \int_{V} \boldsymbol{m} \cdot \boldsymbol{H}_{\rm ext} dV \tag{18}$$

where μ_0 is the permeability of free space [12]. The Zeeman energy reaches its minimum when the magnetic moments m align with H_{ext} [4].

2.1.2 Landau-Lifshitz-Gilbert equation

In an equilibrium state, the magnetic moments m of a ferromagnetic material align parallel to the static effective field $H_{\rm eff}$ (see Fig. 1a), leading to the torque-free condition $m \times H_{\rm eff} = 0$ [5]. However, when a small perturbation is applied, the moments m deviate from alignment with $H_{\rm eff}$. This situation can be compared to a spinning top tilted in a gravitational field: to minimise the energy, the system experiences a $torque\ au$, which drives the precessional motion of m around m around m [4], and is expressed as:

$$\boldsymbol{\tau} = \mu_0 \boldsymbol{m} \times \boldsymbol{H}_{\text{eff}} \tag{19}$$

Since a torque is also described as $\tau = \frac{dJ}{dt}$, where J is the angular momentum, the Landau–Lifshitz equation for ideal systems can be derived from Eq. 2:

$$\frac{d\mathbf{M}}{dt} = \gamma \mu_0 \mathbf{M} \times \mathbf{H}_{\text{eff}} \tag{20}$$

with
$$\gamma = -\frac{ge}{2m_e}$$
.

In practice, energy is dissipated, for example through spin-lattice coupling, defects and other channels. Therefore, the *Landau–Lifshitz equation* must be extended with a phenomenological damping term, characterised by the *Gilbert parameter* α . This leads to the *Landau–Lifshitz–Gilbert (LLG) equation*:

$$\frac{d\mathbf{M}}{dt} = \gamma \mu_0 \left(\mathbf{M} \times \mathbf{H}_{\text{eff}} \right) + \frac{\alpha}{M_{\text{S}}} \left(\mathbf{M} \times \frac{d\mathbf{M}}{dt} \right)$$
 (21)

where $M_{\rm S}$ is the saturation magnetisation [4,5,9]. The damped precessional motion of a single magnetic moment is illustrated in Fig. 1.

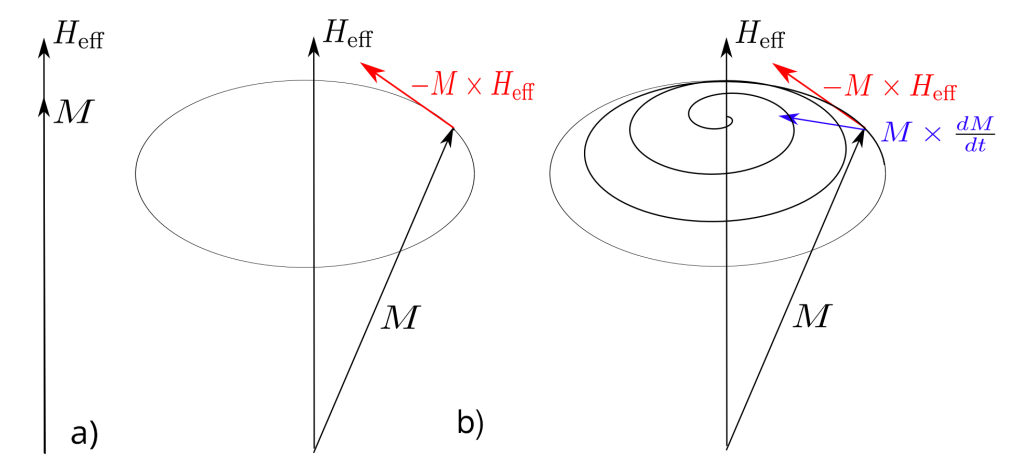


Fig. 1: No precession (a), undamped precession (b), and damped precession (c) of a magnetisation M in the field $H_{\rm eff}$.

2.1.3 Magnetic properties of materials

As already mentioned, the magnetic response of a material to an external field H, and the alignment of the magnetic moments, can be distinguished based on the magnetic susceptibility χ . There are five different categories of magnetic properties: diamagnetism, paramagnetism, ferromagnetism, antiferromagnetism, and ferrimagnetism.

Diamagnetism

Diamagnetic materials do not have a net magnetic moment in the absence of an external magnetic field. Examples of such materials include noble gases, ionic solids, and some semiconductors. According to Lenz's law, the induced magnetic moment in diamagnetic materials opposes the applied magnetic field, resulting in a negative magnetic susceptibility $\chi < 0$. Ideal superconductors are diamagnetic materials with a strong negative magnetic susceptibility of $\chi = -1$ [5]. All materials experience diamagnetic effects; however, these effects are comparatively weak in comparison to the magnetic moments of paramagnetic materials [4,5]

Paramagnetism

In paramagnets, magnetic moments are randomly oriented due to the thermal energy. As a result, the total magnetisation is M=0 at room temperature when no external field is applied. In the presence of a magnetic field, the magnetic moments of the paramagnet begin to align with the field, producing a net magnetisation. The susceptibility χ is inversely proportional to the temperature of the paramagnet and is given by the Curie law of paramagnetism:

$$\chi_{\text{para}} = \frac{C}{T},\tag{22}$$

where C is the material-dependent Curie constant. The degree of alignment of the magnetic moments, and thus stronger magnetisation, increases with the strength of the external field and with a reduction in temperature. Hence, paramagnets exhibit a positive susceptibility, $\chi > 0$ [5].

Ferromagnetism

In ferromagnets, the exchange interactions between neighbouring atoms create magnetic domains — regions where magnetic moments are aligned. With a sufficiently strong external field, the domains gradually align in the direction of the field until all magnetic moments are aligned and the saturation magnetisation $M_{\rm S}$ is reached. This phenomenon gives ferromagnets a strong positive susceptibility,

which for small bias fields is described by the Curie-Weiss law:

$$\chi_{\text{ferro}} = \frac{C}{T - T_{\text{C}}}.$$
 (23)

Here, C is the material-specific Curie constant, and $T_{\rm C}$ is the Curie temperature, at which the thermal energy of the system overcomes the exchange energy, resulting in the saturation magnetisation dropping to zero, $M_{\rm S}=0$. The Curie–Weiss law applies only for $T\gg T_{\rm C}$; hence, above the Curie temperature $T_{\rm C}$, the ferromagnet begins to behave like a paramagnet [4,5].

Antiferromagnetism

In contrast to ferromagnets, the exchange interactions between neighbouring atoms in antiferromagnetic materials result in an antiparallel alignment of the magnetic moments. This arrangement can then be described by two opposing ferromagnetic sublattices with zero total net magnetisation. When the thermal energy exceeds the exchange interaction, the ordered state breaks down, and the material behaves like a paramagnet. For $T > T_{\rm N}$ the temperature dependence of the magnetic susceptibility is given by:

$$\chi = \frac{C}{T + T_{\rm N}}. (24)$$

The critical temperature T_N is called the Néel temperature, below which a sudden change in susceptibility occurs [4,5].

Ferrimagnetism

Ferrimagnetism arises in materials with two or more ferromagnetic sublattices on distinct crystallographic sites. Antiferromagnetic inter-sublattice exchange aligns the sublattices antiparallel, but unequal sublattice moments (from different ions or states) lead to incomplete cancellation and a finite net magnetisation together with a positive susceptibility $\chi>0$. Consequently, ferrimagnets show spontaneous magnetisation and hysteresis, generally with a reduced saturation magnetisation compared with ferromagnets. A characteristic feature is the possible compensation temperature $T_{\rm comp} < T_{\rm C}$, at which the sublattice magnetisations become equal

and the net magnetisation vanishes. Ferrites and garnets are prototypical ferrimagnets, with the most notable representative — YIG (see Chapter 2.3) — being a benchmark magnonic material [4] and the material used in this thesis.

2.2 Spin Dynamics

The precession of spins and magnetic moments is governed by both dipolar and exchange interactions with neighbouring moments, giving rise to collective excitations known as spin waves (SW). The quanta of SW are magnons - bosonic quasiparticles characterised, e.g., by their wavevector \mathbf{k} , wavelength $\lambda = \frac{2\pi}{k}$, linear f or angular frequency $\omega = 2\pi f$, etc. Similar to photon, magnon's energy is given by $E_k = \hbar \omega$, where \hbar is the reduced Planck constant [4, 5, 8, 9].

2.2.1 Ferromagnetic resonance

A special case of excitation is *ferromagnetic resonance* (FMR), in which the spins precess in phase (k=0 SW mode). Experimentally, FMR is driven by an alternating microwave magnetic field $h_{\rm rf} \perp H_{\rm ext}$, and the resonance condition is observed as a peak in absorption/transmission when f matches the eigenfrequency of the system [4,5]. FMR depends not only on the applied magnetic field $H_{\rm ext}$, but also on the sample's shape and orientation due to demagnetising effects.

Linearising the Landau–Lifshitz (Eq. 20) and using the Polder susceptibility yields, for a uniformly magnetised ellipsoid, the Kittel formula for angular frequency:

$$\omega^{2} = \mu_{0}^{2} \gamma^{2} [\boldsymbol{H}_{\text{ext}} + (N_{x} - N_{z}) \boldsymbol{M}_{\text{S}}] [\boldsymbol{H}_{\text{ext}} + (N_{y} - N_{z}) \boldsymbol{M}_{\text{S}}],$$
 (25)

where $N_{\rm x}, N_{\rm y}$ and $N_{\rm z}$ are the three diagonal components of the demagnetising tensor $N_{\rm d}$, and $M_{\rm S}$ is the saturation magnetisation.

A notable case is a thin film, where the demagnetising tensor $N_{\rm d}$ has only one non-trivial component, $N_z=1$ (see Eq. 11). In that case, the Kittel formula is simplified to:

$$\omega_{\text{opp}} = \gamma \mu_0 (|\boldsymbol{H}_{\text{ext}} - \boldsymbol{M}|) \tag{26}$$

if the external magnetic field $oldsymbol{H}_{\mathrm{ext}}$ is perpendicular to the film, and

$$\omega = \gamma \mu_0 \sqrt{\boldsymbol{H}_{\text{ext}}(\boldsymbol{H}_{\text{ext}} + \boldsymbol{M})}$$
 (27)

if $\boldsymbol{H}_{\mathrm{ext}}$ lies in the plane of the film [9].

2.2.2 Spin waves of thin films

Beyond the uniform FMR modes, non-uniform spin precession ($\mathbf{k} \neq 0$) with a finite phase difference between neighbouring spins gives rise to spin waves. In the long-wavelength regime (millimetre to micrometre scale), their properties are dominated by dipolar interactions, whereas in the short-wavelength regime (sub-micrometre to nanometre scale) exchange interactions are the primary influence.

The dispersion relation $\omega(k)$ relates the SW frequency to its wavevector. It primarily depends on both the magnitude and the direction of k, the film thickness, and the angle between k and the magnetisation M. In magnetically ordered media, three principal magnetostatic SW geometries are distinguished: backward volume magnetostatic spin waves (BVMSW), Damon-Eshbach (DE)/ magnetostatic surface spin waves (MSSW) and forward volume magnetostatic spin waves (FVMSW). For any other orientation of H and H0, the resulting SW is a hybrid of these three types [2, 8].

One important property of SWs is their *group velocity*, which describes the rate at which information or energy is transported by the wave, and is defined as:

$$v_{\rm gr} = \frac{2\pi\partial f}{\partial k} = \frac{\partial\omega}{\partial k} \tag{28}$$

The group velocity directly determines the SW *free path* - the distance over which a SW decays to 1/e of its amplitude:

$$l_{\text{free}} = v_{\text{gr}}\tau \tag{29}$$

Consequently, the *spin wave lifetime* τ is the characteristic time over which the amplitude of a SW decays by a factor of 1/e due to damping processes, such

as Gilbert damping, inhomogeneous broadening, magnon-magnon or magnonphonon scattering. For a spherical region in an infinite medium and considering only intrinsic Gilbert damping, the lifetime is [1]:

$$\tau_0 = \frac{1}{\alpha \cdot 2\pi f}.\tag{30}$$

• Backward Volume Magnetostatic Spin Waves (BVMSW, $k\|M$)

Applying an external magnetic field $H_{\rm ext}$ in the plane of a saturated magnetic medium leads to BVMSWs excitation, characterised by the wavevector k parallel to the field direction. For dipole-dominated interactions in a thin film of thickness d, the dispersion relation can be explicitly solved for ω , as derived by Kalinikos and Slavin. For the lowest-order mode (n=0), the equation is:

$$\omega_{\text{BVMSW}}(k) = \sqrt{\omega_{\text{H}} \left[\omega_{\text{H}} + \omega_{\text{M}} \left(\frac{1 - e^{-kd}}{kd} \right) \right]}$$
(31)

where $\omega_{\rm H}=\gamma\mu_0H_0$ and $\omega_{\rm M}=\gamma\mu_0M_{\rm S}$, with γ being the gyromagnetic ratio and H_0 the effective internal field [4,6,8]. Notably, this results in a negative group velocity, $v_{\rm gr,BVMSW}=\frac{\partial\omega}{\partial k}<0$ [4], which is derived for an applied magnetic flux density B as:

$$v_{\text{gr,BVMSW}} = \frac{\gamma \sqrt{B} \mu_0 M_{\text{s}}}{2} \cdot \frac{e^{-kd} + kd \cdot e^{-kd} - 1}{k^2 d \sqrt{B + \frac{\mu_0 M_{\text{s}} (1 - e^{-kd})}{kd}}}$$
(32)

• Damon-Eshbach Spin Waves (DE, $k \perp M$)

Damon-Eshbach SW mode propagates in magnetic medium when an external inplane field $H_{\rm ext}$ is applied orthogonally to the SW wavevector k. Contrary to BV, the amplitude of DE modes decreases with increasing penetration depth into the sample, indicating that DE modes primarily propagate along the surface of the film. The dispersion relation of DE can be approximated by: [6,8]

$$\omega_{\rm DE} = \sqrt{\omega_{\rm H}(\omega_{\rm H} + \omega_{\rm M}) + \frac{\omega_{\rm M}^2}{4} \left[1 - e^{-2kd}\right]}$$
 (33)

From the discussed magnetisation configurations, DE has the highest efficiency,

but is nonreciprocal. This means that the propagation of the excited DE is unidirectional in films [8]. The derived group velocity of DE can be expressed as:

$$v_{\rm gr,DE} = \frac{\gamma \mu_0^2 M_{\rm s}^2}{2} \cdot \frac{d e^{-2kd}}{\sqrt{-\mu_0^2 M_{\rm s}^2 e^{-2kd} + (\mu_0 M_{\rm s} + 2B)^2}}$$
(34)

• Forward Volume Magnetostatic Spin Waves (FVMSW, out-of-plane $k \perp M$)

An external magnetic field $H_{\rm ext}$ applied perpendicular (out-of-plane) to the thin film will induce FVMSWs, with the dispersion relation as: [4,8]

$$\omega_{\text{FVMSW}} = \sqrt{\omega_{\text{H}} \left[\omega_{\text{H}} + \omega_{\text{M}} \left(1 - \frac{1 - e^{-kd}}{kd} \right) \right]}$$
(35)

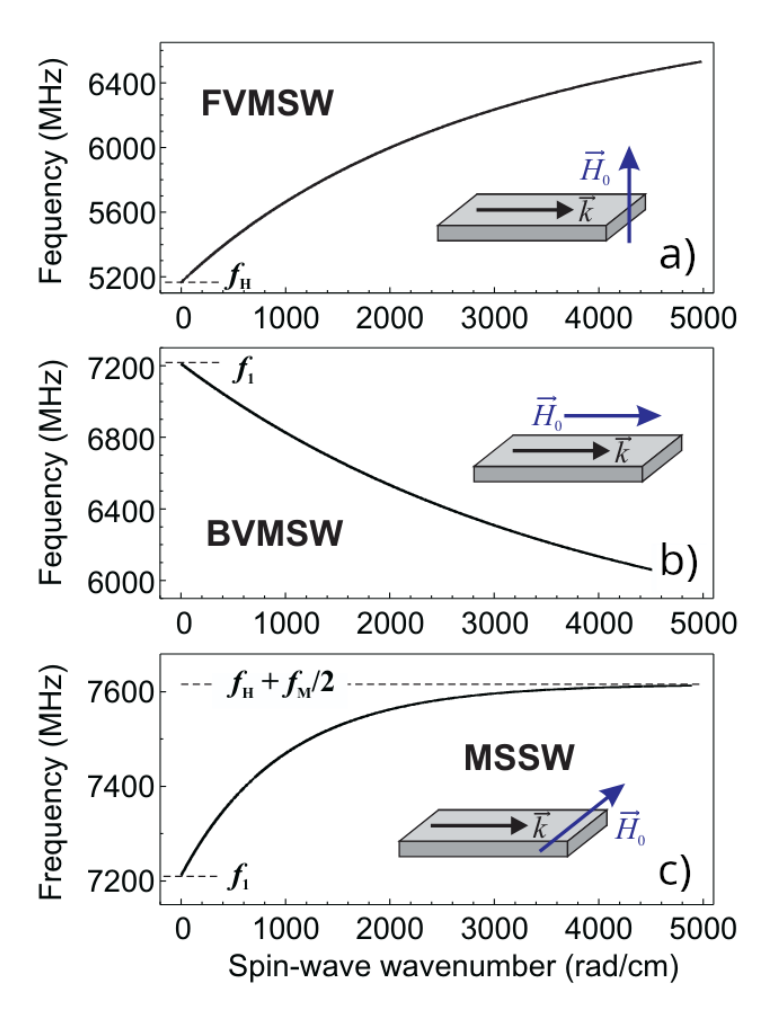


Fig. 2: Dispersion relations of a) FVMSW, b) BVMSW, and c) MSSW/DE, derived from equations 31, 33 and 35 respectively, for a bias magnetic field $H_0 \approx 146.8 \mathrm{kA} \, \mathrm{m}^{-1}$, a saturation magnetisation $M_\mathrm{S} \approx 0.175 \mathrm{T}$, and a film thickness of $d = 5 \, \mu \mathrm{m}$. (Taken from [8].)

2.2.3 Propagating Spin-Wave Spectroscopy

Spin waves are commonly excited and detected using antennas in magnetic thin films. After the sample has been magnetised by an external magnetic field, an alternating current (AC) is applied to the excitation antenna. The oscillating magnetic field created by the antenna acts on the magnetic moments inside the sample, resulting in an applied torque. If the frequency of the current matches the resonance condition of the material, the amplitude of the magnetic moments increases in the direction perpendicular to the magnetic field, and SW is generated. If the SW free path is longer than the distance between the antennas, the signal reaches detection antenna and follows identical, reverse process of SW to AC conversion [8].

Excitation via microstrip

The efficiency and excitation profile depend on the shape of the antenna, and are given by the Fourier transform of the current density. The simplest example of an excitation antenna is a microstrip, which results in transmitted SWs, as shown in Fig. 3 [4].

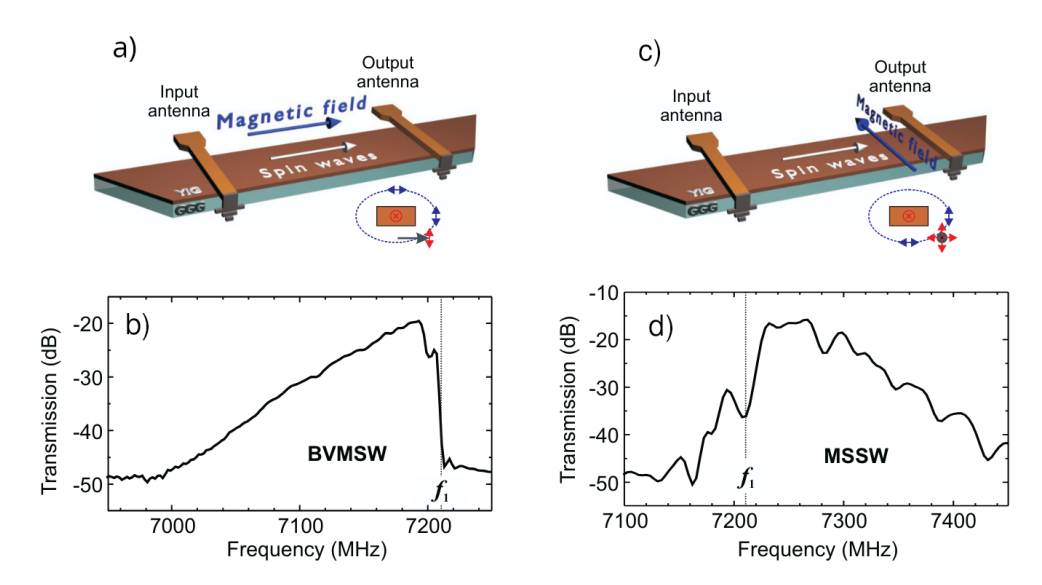


Fig. 3: Microstrip setup for SW excitation in YIG/GGG samples: a) setup for BVMSW, and c) setup for MSSW; b) and d) show example transmission characteristics for BVMSW and MSSW. (Adapted from [8].)

Microstrips are viable at the macroscale due to their strong coupling between electromagnetic and spin waves. Previous measurements of YIG samples with thick-

nesses of a few micrometres showed that the excitation bandwidth increases with the thickness and saturation magnetisation of the sample, but decreases with a stronger bias field. In addition, stronger bias field and larger thickness result in a higher maximum radiation resistance [1]. The field created by a microstrip antenna is illustrated in Fig. 4.

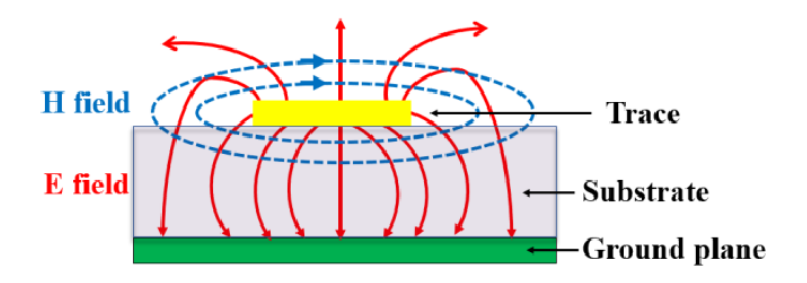


Fig. 4: Electric field (E) and magnetic field (H) distribution in the cross-section of a microstrip transmission line. (Taken from [13].)

Scattering matrix

For high-frequency measurements, a VNA typically controls and measures both the incoming and outgoing signals. A VNA has two or more ports, through which signals are transmitted and received. The signals sent from a port are incident waves, which are partially reflected and detected by that port. Ideally, the remaining portion of the signal is fully transmitted and detected by the other port [7].

The transmission and reflection characteristics between two ports can be described using the scattering matrix, S_{ij} . If a_1 and a_2 are the incident signals at ports 1 and 2, and b_1 and b_2 are the resulting signals, then:

$$\begin{pmatrix} b_1 \\ b_2 \end{pmatrix} = \begin{pmatrix} S_{11} & S_{12} \\ S_{21} & S_{22} \end{pmatrix} \begin{pmatrix} a_1 \\ a_2 \end{pmatrix}$$

$$\tag{36}$$

Here, S_{11} and S_{22} represent the reflection coefficients at ports 1 and 2, respectively, and S_{21} and S_{12} represent the transmission coefficients. Each coefficient defines how an incident wave at one port influences the signal received at another [7].

$$S_{11} = \frac{Reflected}{Incident} = \frac{b_1}{a_1} \bigg|_{a_1=0} \qquad S_{12} = \frac{Reflected}{Incident} = \frac{b_1}{a_2} \bigg|_{a_2=0}$$

$$S_{21} = \frac{Transmitted}{Incident} = \frac{b_2}{a_1} \bigg|_{a_1=0} \qquad S_{22} = \frac{Transmitted}{Incident} = \frac{b_2}{a_2} \bigg|_{a_2=0}$$
(37)

One notable quality of a VNA is its ability to eliminate systematic errors, such as power loss in cables, through user calibration. SOLT (Short–Open–Load–Thru) calibration measures four well-known standards to solve the error model, set the reference plane at the sample ports, and establish the reference impedance, which is usually set at $50~\Omega$ (discussed in the next section). After SOLT calibration, the reported S-parameters ideally reflect only the device under test, with minimal interference. This makes VNAs one of the most accurate RF test instruments available [7].

Characteristic impedance and coaxial cable

In high-frequency applications, coaxial cables are commonly used to minimise signal loss due to the skin effect and to maintain a consistent impedance. To understand the behaviour of the electromagnetic fields inside a coaxial cable, it is helpful to first consider the simplified model of two parallel conductors carrying equal and opposite currents, I and -I. This setup can be modelled using a distributed-element circuit (Fig. 5), where the cable segment of length Δx is characterised by R', L', G' and C', representing resistance, inductance, conductance, and capacitance per unit length.

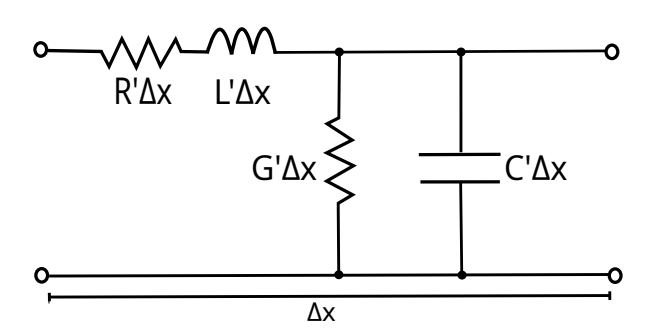


Fig. 5: Corresponding circuit diagram of two parallel cables

If an alternating current with angular frequency ω is applied, the characteristic impedance z_0 is then:

$$z_0 = \frac{U}{I} = \sqrt{\frac{R' + i\omega L'}{G' + i\omega C'}}$$
(38)

A coaxial cable consists of an inner conductor surrounded by a concentric outer conductor, forming a cylindrical geometry that confines both the electric field (radial) and the magnetic field (azimuthal), as shown in Fig. 6.

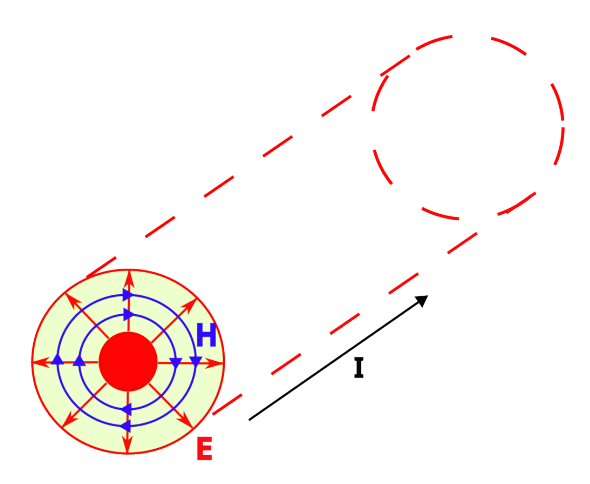


Fig. 6: Electric and magnetic field in a coaxial cable.

The impedance of a coaxial line depends on its geometry and materials. Minimum signal attenuation occurs around 77Ω , while minimum power dissipation (resistive losses) occurs near 30Ω . Therefore, a compromise value of 50Ω is widely adopted for laboratory and RF equipment. To ensure efficient signal transfer, it is important to match the impedances of all connected components. The reflection coefficient Γ between two components with impedances z_0 and z_1 is given by:

$$\Gamma = \frac{z_1 - z_0}{z_1 + z_0} \tag{39}$$

and with $|\Gamma|^2$ giving the power reflection coefficient. Impedance mismatches result in signal reflections, reducing the measurement accuracy [14].

2.3 Yttrium Iron Garnet (YIG)

For spin-wave excitation in magnonic experiments, yttrium iron garnet (YIG, $Y_3Fe_5O_{12}$) is the preferred material due to its having the lowest known magnetic damping, narrowest FMR linewidth, wide frequency range, and long spin-wave propagation lengths [6, 15]. It is commonly grown on a gadolinium gallium garnet (GGG) substrate, which possesses a similar lattice to YIG, ensuring high-quality films.

YIG is a ferrimagnetic insulator, composed of two magnetically coupled sublattices of Fe^{3+} ions located on tetrahedral and octahedral sites. These sublattices are aligned antiparallel due to antiferromagnetic exchange interactions. Per for-

mula unit, three Fe^{3+} ions occupy tetrahedral sites and two occupy octahedral sites, yielding a net magnetic moment of $5~\mu_{\rm B}$ and a room-temperature saturation magnetisation of $M_{\rm S}=143~{\rm kA~m^{-1}}$ [9]. A significant strength of YIG is its weak spin–orbit interaction, which leads to low magnetic losses and, consequently, to exceptionally low damping [3,8] (Gilbert damping constant, typically $\alpha\approx 5\cdot 10^{-5}$). This enables spin-wave propagation over distances from micrometres up to several millimetres, depending on the frequency, mode type, and film thickness [8].

YIG is a ferrimagnetic insulator, composed of two magnetically coupled sublattices of Fe^{3+} ions located on tetrahedral and octahedral sites. These sublattices are aligned antiparallel due to antiferromagnetic exchange interactions. Per formula unit, three Fe^{3+} ions occupy tetrahedral sites and two occupy octahedral sites, yielding a net magnetic moment of $5~\mu_{\rm B}$ and a room-temperature saturation magnetisation of $M_{\rm S}=143~{\rm kA~m^{-1}}$ [9].

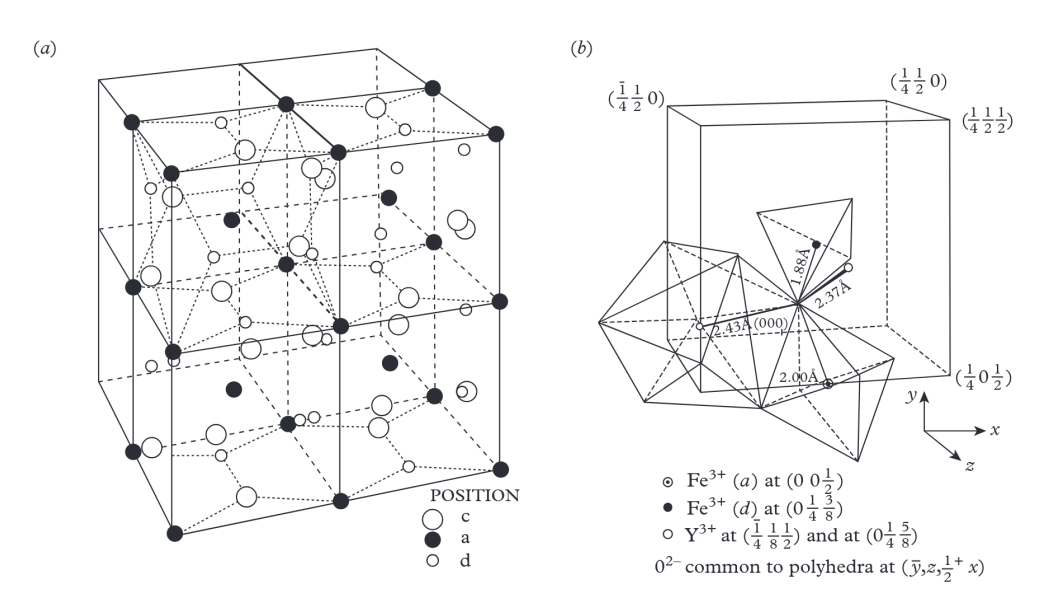


Fig. 7: Structure of Yttrium Iron Garnet ($Y_3Fe_5O_{12}$). (Taken from [5].)

3 Setup upgrade

The excitation of SW is highly dependent on the magnetic field within the sample. Therefore, it is important to accurately determine the external field that interacts with the magnetic moments inside the sample. For precise and reliable measurement, it is crucial to position the Hall probe as close as possible to the sample.

Present limitations

In the current setup, the mounting point for the Hall probe holder is located behind the electromagnet. This makes access and adjustment difficult, resulting in suboptimal placement of the Hall probe. Furthermore, the probe is rotated into its final position via an adjustable rotary joint, which can lead to interference with the sample and complicate positioning, as two axes are adjusted simultaneously.

In the case of measurements using nanoscale films, the sample holder completely blocks access to the Hall probe mounting point. As a compromise, the holder is temporarily attached to one side of the magnetic core, resulting in approximate and less reliable field measurements.

Future setup

To improve the setup, a hole has been drilled into the top plate of the electromagnet, through which the Hall probe can be lowered. However, the diameter of the hole does not accommodate the default size of the probe holder. Therefore, a new holder has been designed using *Autodesk Inventor Professional 2026*. The design is shown in Fig. 8.

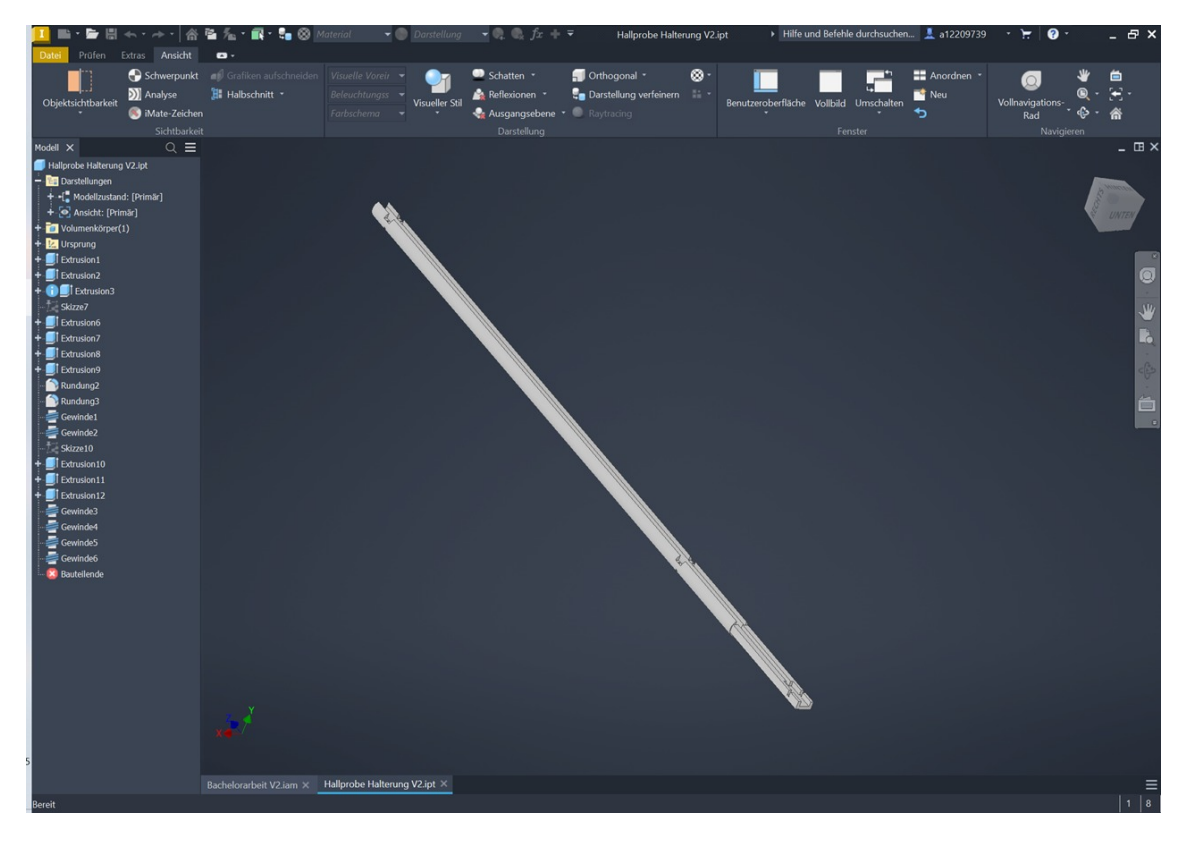


Fig. 8: Design of the Hall probe holder in Autodesk Inventor Professional 2026.

The securing mechanism is inspired by the previous holder, where the Hall probe is placed in a narrow channel and fastened using small metal plates and screws. The elongated cylindrical design provides additional rotational freedom. The screw holes are designed for standardised M1.2 screws to ensure easier sourcing and reduced cost.

The new design allows a Hall probe with a thickness of $6\,\mathrm{mm}$ to be inserted through the $11\,\mathrm{mm}$ -diameter hole in the electromagnet, enabling more accurate and stable positioning for field measurements.

4 Methodology

4.1 Experimental setup

The experimental setup used for the measurements is shown in Fig. 9. It includes the vector network analyser (VNA) "R&S® ZNA67" from *Rohde & Schwarz*, with a frequency range of $10\,\mathrm{MHz}$ – $67\,\mathrm{GHz}$. The external magnetic field is supplied by a "GMW 3473-70" H-frame electromagnet (accuracy: $\pm 0.2\,\mathrm{mT}$), with a pole diameter of $150\,\mathrm{mm}$ and a maximum current of $70\,\mathrm{A}$.

The excitation antennas used are microstrips with a spacing of $(16.5\pm0.5)\,\mathrm{mm}$, connected to the VNA via two Sucoflex 104 coaxial cables from *HUBER+SUHNER*. Three waveguides are employed, each consisting of YIG/GGG film with a width of $2\,\mathrm{mm}$. The films differ in thickness, being $4.1\,\mu\mathrm{m}$, $7.78\,\mu\mathrm{m}$, and $22.83\,\mu\mathrm{m}$.

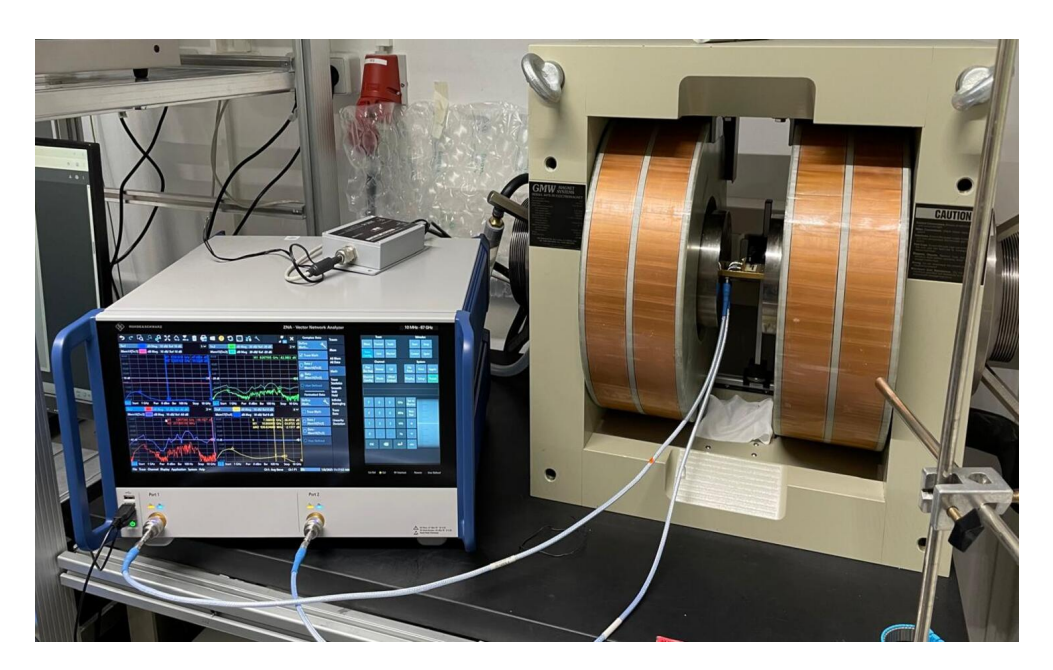


Fig. 9: Experimental setup: antenna and waveguide placed inside the electromagnet (right), connected via coaxial cables to the VNA (left).

The antenna holder is clamped horizontally and aligned in-plane with the magnetic field. The samples are placed perpendicularly on top of the antenna, resulting in either the BVMSW or DE configuration, depending on the orientation of the holder. To avoid interference between the magnet poles and the coaxial cables, 90° adapters are used in the DE configuration, as shown in Fig. 10. The magnetic

field is measured and calibrated using a Hall probe in its default holder, positioned as close as possible to the waveguide.

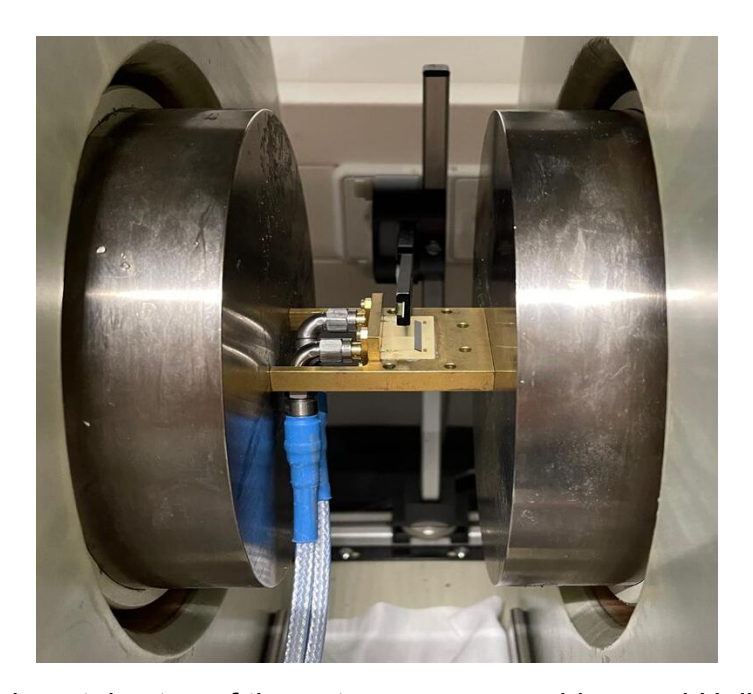


Fig. 10: Experimental setup of the antennas, waveguides, and Hall probe for the DE configuration inside the electromagnet.

4.2 Measurements

The VNA was calibrated using a SOLT calibration kit over the frequency range $1-25\,\mathrm{GHz}$, with a frequency step size of $1\,\mathrm{MHz}$, resulting in $24\,000$ measured points. The transmission parameters S_{21} and S_{12} , as well as the reflection parameters S_{11} and S_{22} at ports 1 and 2, were measured under the following conditions:

All three waveguides were measured in both the BVMSW and DE configurations, with an input power of $0\,\mathrm{dBm}$, a frequency step of $1\,\mathrm{MHz}$, and a bandwidth of $1\,\mathrm{kHz}$. The first set of measurements covered the frequency range $1{\text -}10\,\mathrm{GHz}$, with the applied external field ranging from 0 to $275\,\mathrm{mT}$ in $25\,\mathrm{mT}$ steps. An exception was made for the $7.78\,\mu\mathrm{m}$ -thick film in the DE configuration, for which only approximate $25\,\mathrm{mT}$ steps were used, due to a lack of fine control of the electromagnet caused by technical at that time.

The measurements at $0\,\mathrm{mT}$ were used as a reference for noise subtraction, resulting in 11 excitations measured for each configuration in the $1-10\,\mathrm{GHz}$ range.

The second set of measurements covered the frequency range $10-25\,\mathrm{GHz}$, using a reference field of $270\,\mathrm{mT}$ for subtraction. Excitations were measured with an applied field ranging from 300 to $800\,\mathrm{mT}$ in $25\,\mathrm{mT}$ steps, resulting in 21 measurements for each sample in each configuration.

Additional measurements were taken for the $4.1\,\mu\mathrm{m}$ -thick film at $75\,\mathrm{mT}$ and $350\,\mathrm{mT}$, with a reduced frequency step size of $100\,\mathrm{kHz}$, in order to obtain an extended delay time spectrum and verify the recorded data.

4.3 Analysis

Antenna wave-vector selectivity

The current density $J_{\rm exc}$ is used in combination with the theoretical dispersion relation to compare the theoretical excitation with the experimental measurements. For the microstrip antennas used, the current density $J_{\rm exc}$ is given by:

$$J_{\rm exc}(k) = \left(\frac{\sin\left(\frac{ka}{2}\right)}{\frac{ka}{2}}\right)^2 \tag{40}$$

with $a=60~\mu\mathrm{m}$ being the width of the excitation antennas.

Signal conditioning and units

The complex data were converted into amplitude and subsequently into decibels using the relation:

$$S_{\text{ii, dB}} = 20 \cdot \log_{10} |S_{\text{ii}}|,$$
 (41)

and the power ratio was determined by:

$$P_{\rm dB} = 10 \cdot \log_{10} P \tag{42}$$

Background removal and time gating

For the measured signals with applied magnetic fields of 75 mT, 78.7 mT, and 350 mT, a time-gating procedure was applied. An inverse fast Fourier transform (IFFT) was performed on the S_{12} and S_{21} signals to extract the delay time of the

measured excitations at each frequency.

A significant portion of the systematic error originates from electromagnetic (EM) leakage from the excitation antennas. Since EM waves travel at the speed of light, they produce unwanted excitations at much shorter delay times compared to propagating SW. Time gating allows for effective suppression of this leakage by isolating only those signals whose delay times correspond to the PSWS itself. A fast Fourier transform (FFT) is then applied to transform the gated signal back into the frequency domain, allowing for additional noise reduction in the subsequent analysis [16].

Figures of merit

The insertion loss is determined by extracting the maximum of the leakage-removed transmission signal, with the reference point for total transmission set at $0~\mathrm{dB}$.

The bandwidth is calculated by identifying the frequency range over which the signal remains above *insertion loss* -3 dB, corresponding to at least half the power relative to the peak signal.

The dynamic range is obtained as the difference between the insertion loss and the noise level. To estimate the noise level, a reference point at a frequency offset of $300~\mathrm{MHz}$ above or below the frequency of the insertion loss is used. These three characteristics are illustrated in Fig. 11.

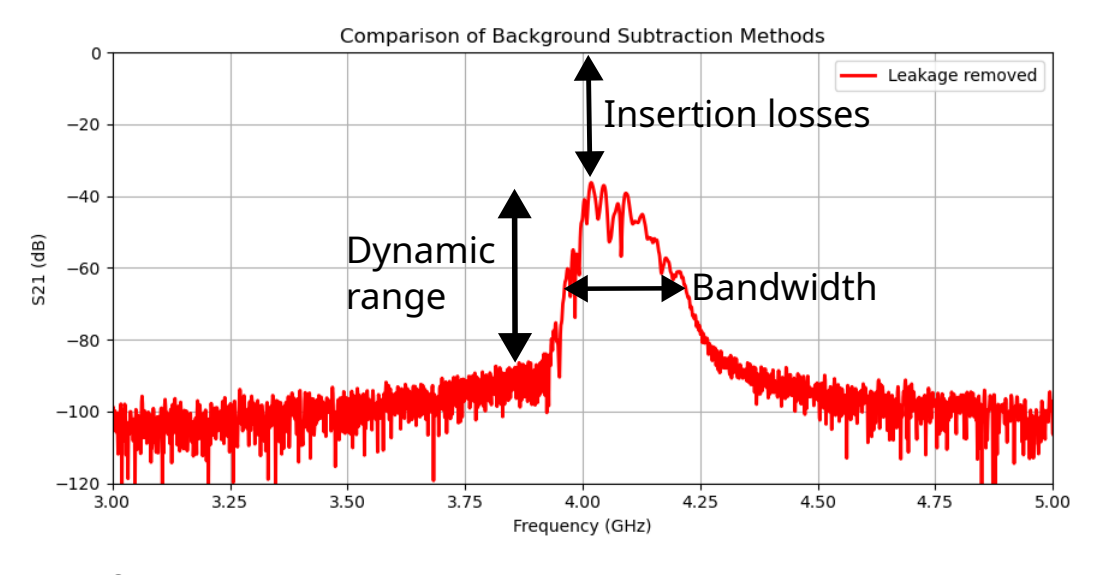


Fig. 11: Characteristics: insertion loss, bandwidth, and dynamic range (dynamic range not at *insertion loss* $-3~{\rm dB}$ for improved visibility).

Computational tools

The raw data and theoretical calculations were processed using the Python programming language, along with the following key packages: os, re, numpy, scipy, and matplotlib. For grammar and syntax corrections, the AI models DeepL and ChatGPT were used. However, all content — including data, information, and conclusions — are my own or taken from cited sources.

5 Results

This chapter presents the results obtained from the extracted experimental data, as well as the corresponding theoretical analysis for comparison, including the analysis of the SW excitation frequency at different magnetic field strengths, various thicknesses, and magnetisation geometries. Furthermore, the delay time, insertion losses, bandwidth, and dynamic range are determined, along with the ferromagnetic resonance (FMR) frequencies over a wide range of magnetic field strengths. The data were extracted from the measured transmission coefficients S_{21} and S_{12} for all three samples and both magnetisation geometries.

This and the following Discussion section show selected exemplary cases. For all other samples, magnetisation geometries and frequency ranges, the measurements and their interpretation were consistent with the representative analysis unless noted otherwise."

5.1 Overview: FMR, dispersion relation

The Spin-wave propagation spectra are represented by the $22.83\,\mu\mathrm{m}$ -thick YIG film for DE and BV from $1\,\mathrm{GHz}$ – $25\,\mathrm{GHz}$ in the Figs. 12-15.

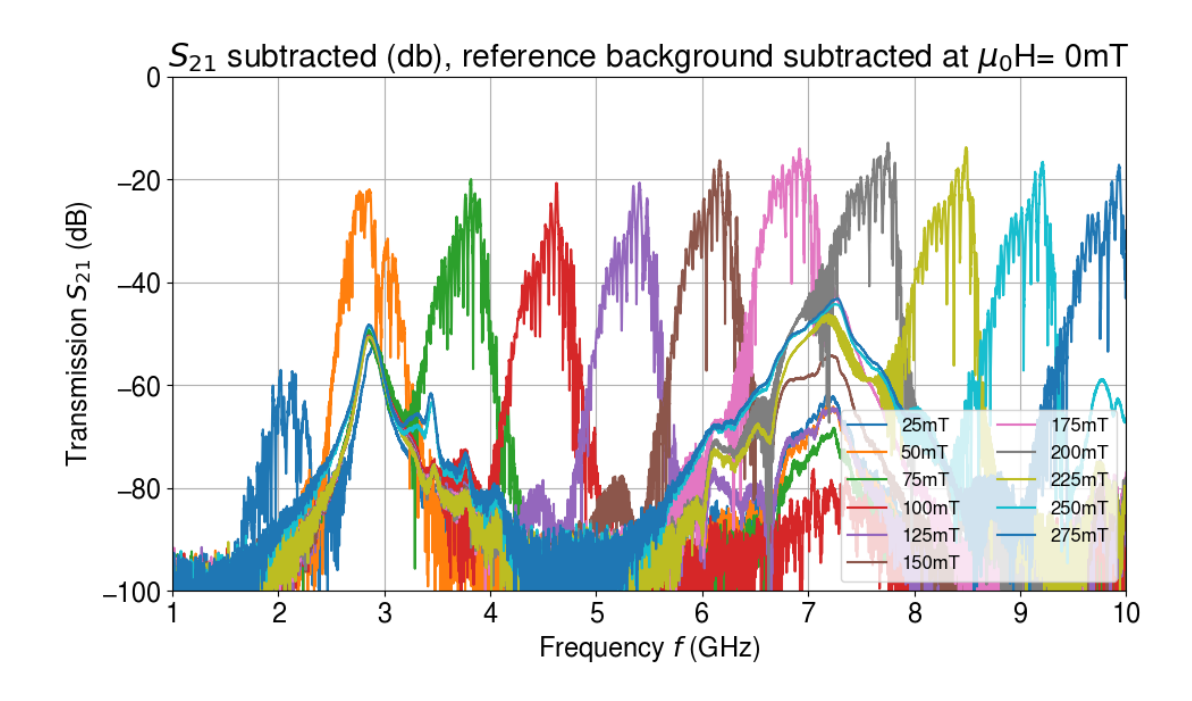


Fig. 12: S_{21} propagating spin-wave spectrum of a $22.83\mu m$ -thick YIG film in the BV configuration, with the 0mT transmission signal subtracted. Measured over a frequency range of 1-10GHz and a magnetic field range of 25-275mT.

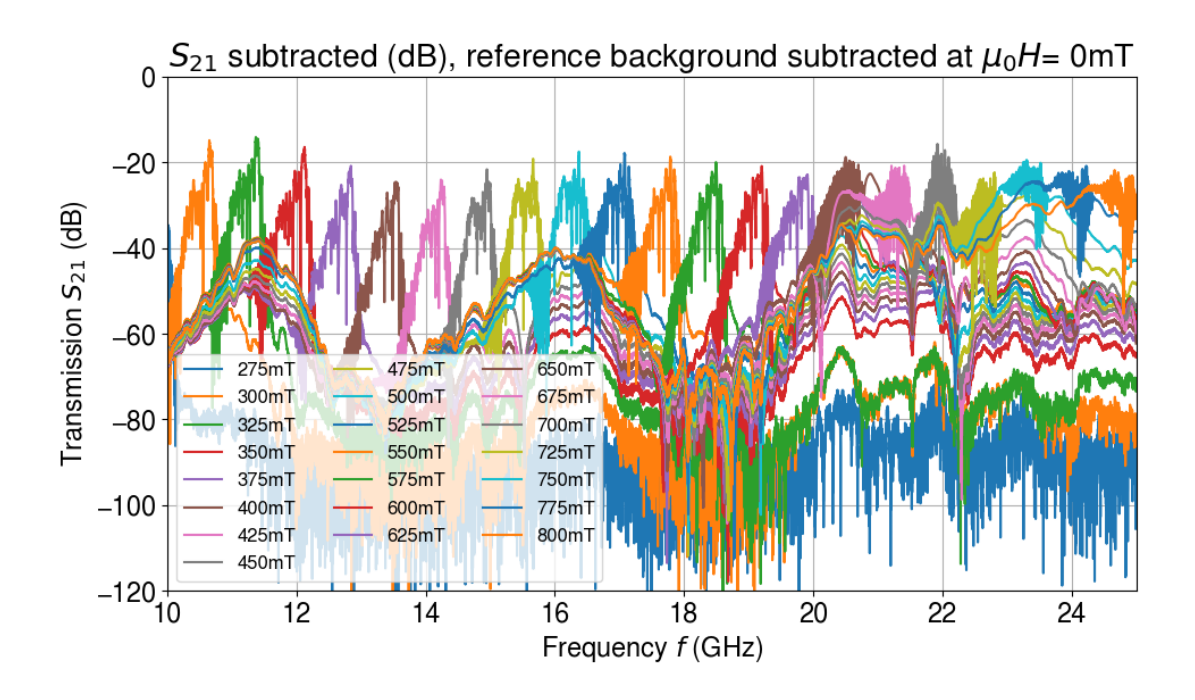


Fig. 13: S_{21} propagating spin-wave spectrum of a $22.83\mu\mathrm{m}$ -thick YIG film in the BV configuration, with the $270\mathrm{mT}$ transmission signal subtracted. Measured over a frequency range of $10-25\mathrm{GHz}$ and a magnetic field range of $300-800\mathrm{mT}$.

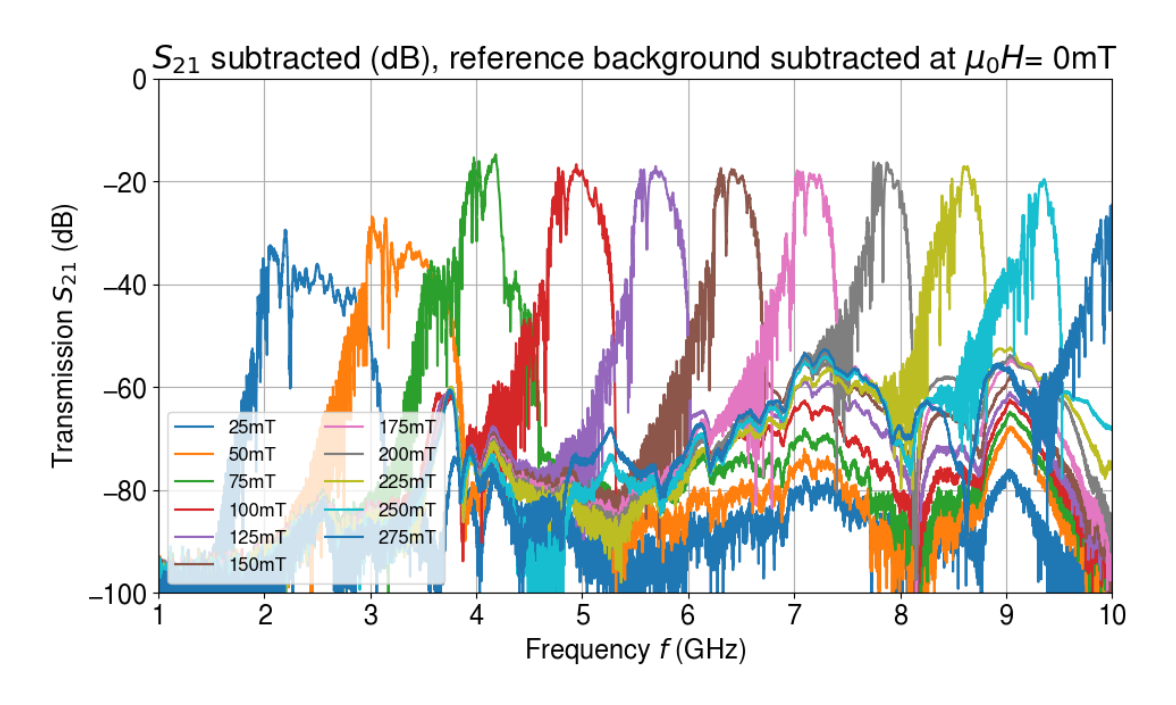


Fig. 14: S_{21} propagating spin-wave spectrum of a $22.83\mu\mathrm{m}$ -thick YIG film in the DE configuration, with the $0\mathrm{mT}$ transmission signal subtracted. Measured over a frequency range of $1-10\mathrm{GHz}$ and a magnetic field range of $25-275\mathrm{mT}$.

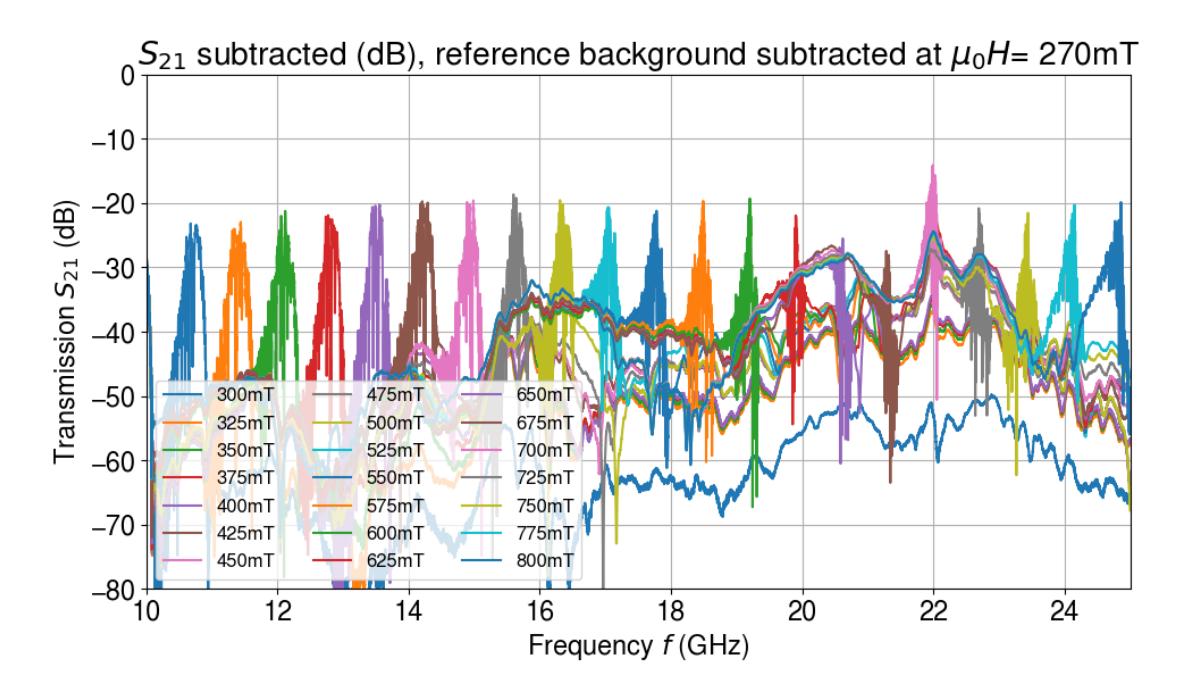


Fig. 15: S_{21} propagating spin-wave spectrum of a $22.83\mu\mathrm{m}$ -thick YIG film in the DE configuration, with the $270\mathrm{mT}$ transmission signal subtracted. Measured over a frequency range of $10-25\mathrm{GHz}$ and a magnetic field range of $300-800\mathrm{mT}$.

The frequency of the distinctive resonance peak corresponds to the ferromagnetic resonance at each applied magnetic field. The extracted FMR frequencies for all

the measured samples are compiled in Appendix Table 4. Figure 16 shows the FMR frequency for the $22.83~\mu\mathrm{m}$ -thick YIG sample in the DE geometry, plotted alongside the prediction from the Kittel formula (Eq. 27).

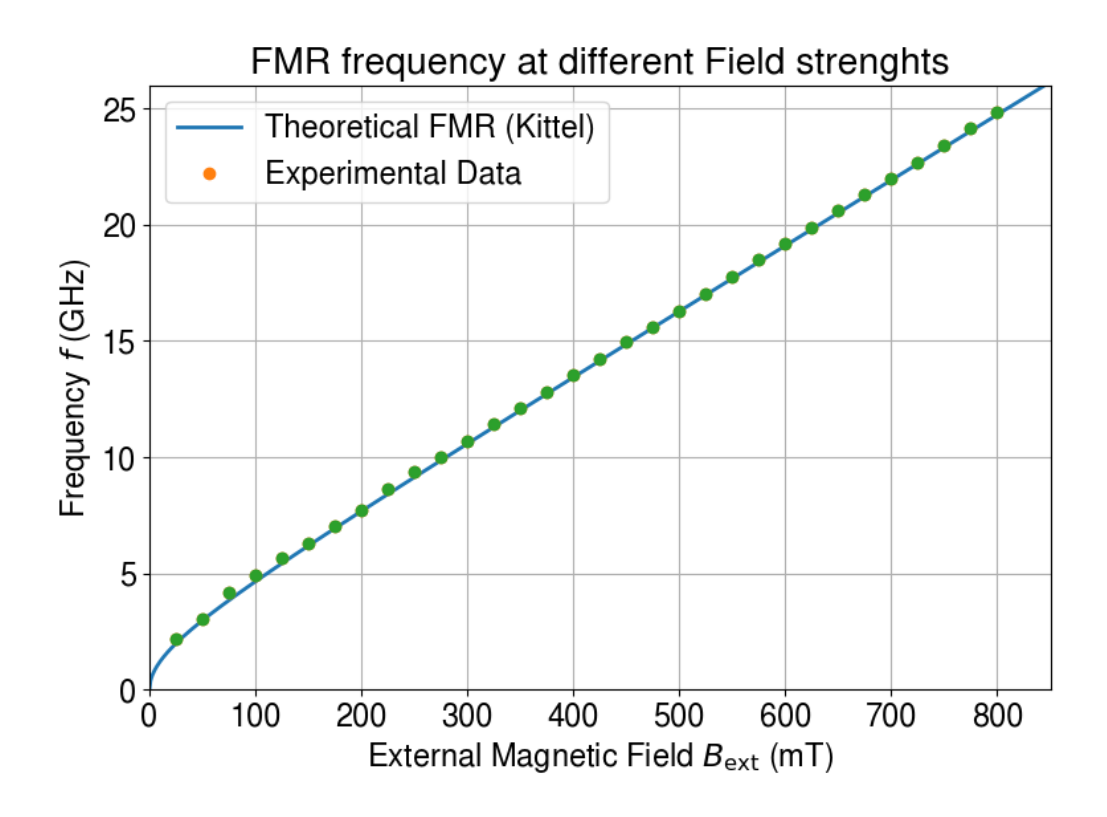


Fig. 16: FMR frequency for a $22.83 \mu m$ -thick YIG sample in the DE configuration, shown in comparison with the Kittel equation (Eq. 27).

The theoretical dispersion relation is calculated using Eqs. 31 and 33, together with the relation $f=\frac{\omega}{2\pi}$. The resulting dispersion curves for all three measured film thicknesses are shown in Fig. 18 for an external magnetic field of $75~\mathrm{mT}$. In Figs. 18 and 19, the experimental excitation spectra are compared with both the antenna's excitation profile and the theoretical dispersion relation for a $7.78~\mu\mathrm{m}$ -thick YIG film in the BV and DE configurations, respectively. A slight adjustment of the magnetic field was necessary to achieve agreement between the experimental data and theoretical calculations — the rationale for this adjustment is presented in the Discussion section.

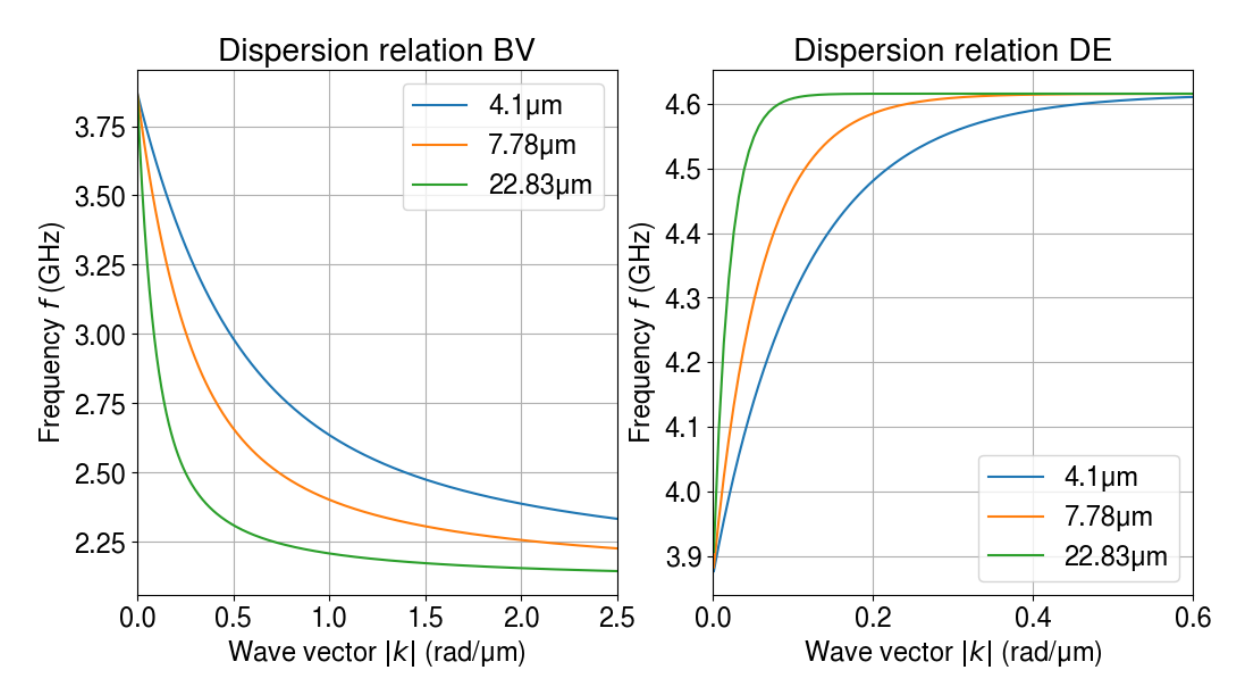


Fig. 17: Theoretical dispersion relation for $4.1\mu\mathrm{m}$, $7.78\mu\mathrm{m}$, and $22.83\mu\mathrm{m}$ -thick YIG films at $B_{\mathrm{ext}}=75\mathrm{mT}$.

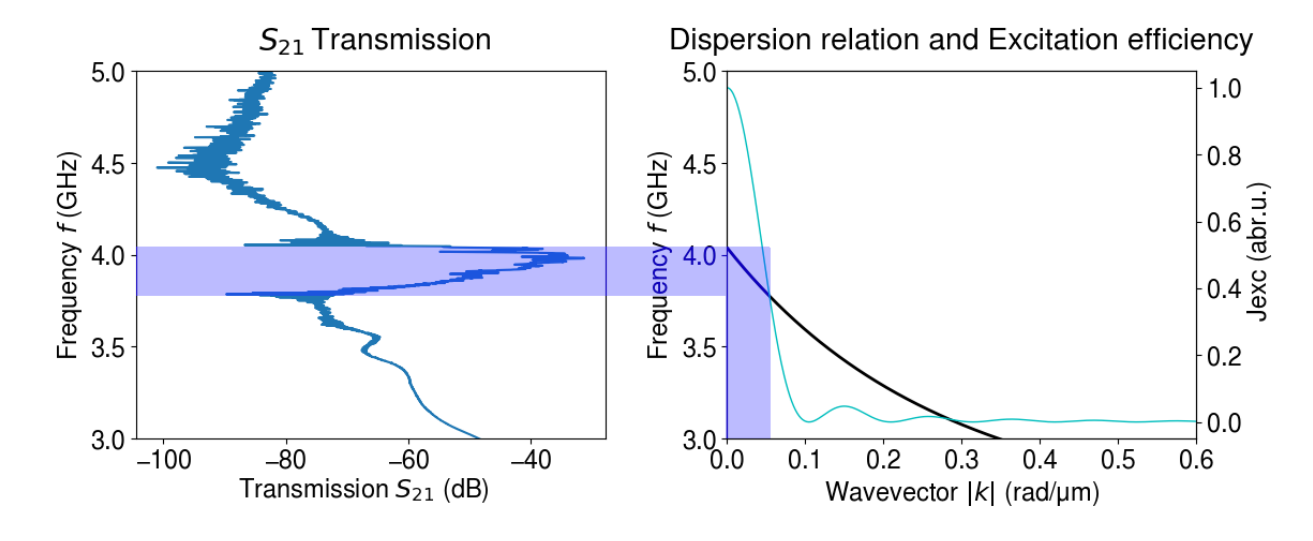


Fig. 18: Measured excitation efficiency of a $7.78\mu\mathrm{m}$ -thick YIG film in the BV configuration compared to the theoretical dispersion relation and excitation profile. The magnetic field was set to $75\mathrm{mT}$ for the experiment, but the calculations were adjusted to $81\mathrm{mT}$.

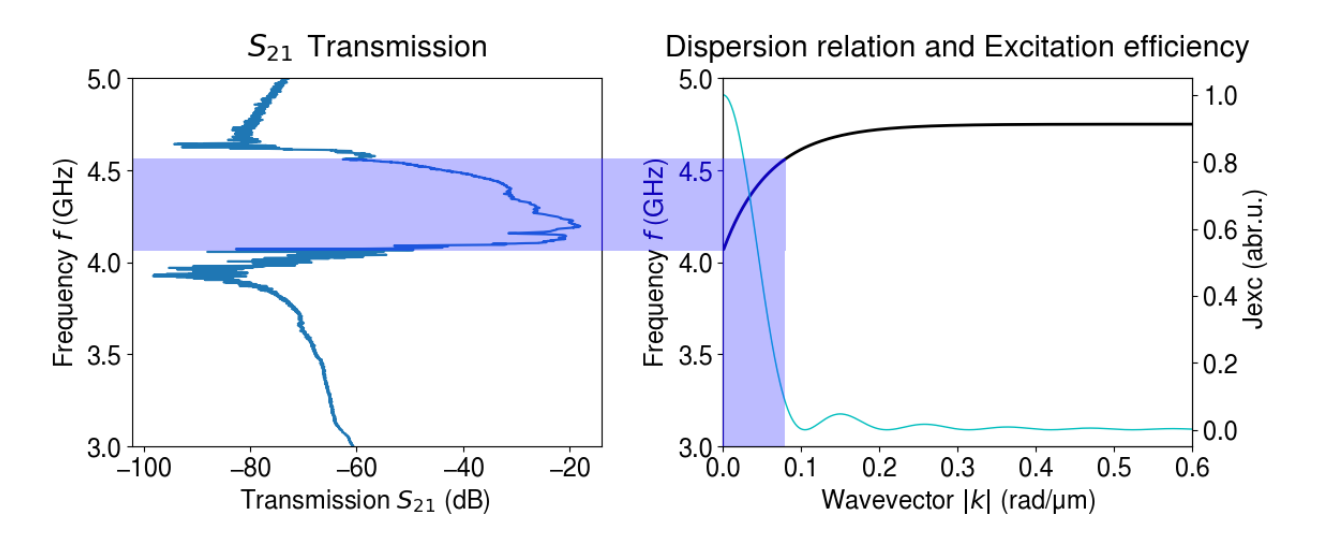


Fig. 19: Measured efficiency of a $7.78\mu\mathrm{m}$ -thick YIG film in the DE configuration compared to the theoretical dispersion relation and excitation profile. The magnetic field was set to $78.7\mathrm{mT}$ for the experiment, but the calculations were adjusted to $81.7\mathrm{mT}$.

5.2 FFT: delay time, group velocity and characteristics

The delay time of the spin-wave signal (shown in red) was extracted using IFFT, whereas other contributions (in black), most notably the electromagnetic peak within the first few nanoseconds, were identified and removed. An example of the delay time, as well as the resulting signal improvement, can be seen in Fig. 20 for a $7.78\mu\mathrm{m}$ -thick film in the BV configuration with a bias field of $75\mathrm{mT}$.

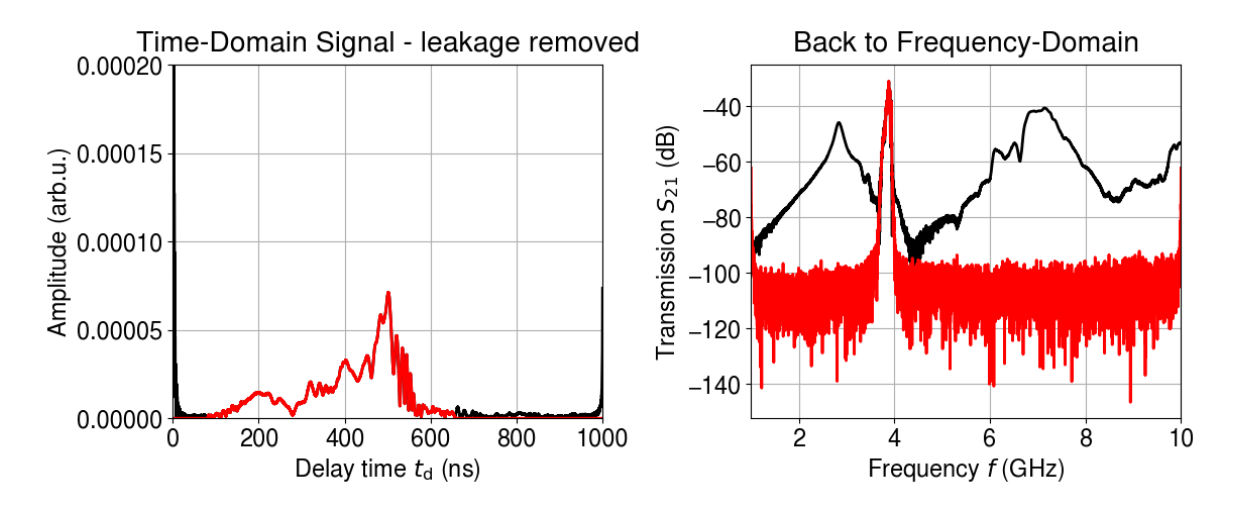


Fig. 20: Delay time and leakage removal via FFT of a $7.78\mu\mathrm{m}$ -thick film in the BV configuration with an external magnetic field of $75\mathrm{mT}$. The original data is shown in black and the leakage-removed data in red.

The expected group velocity is shown in Figs. 21 and 22 and is calculated by taking the derivative of Eqs. 31 and 33 with respect to k. The corresponding expected delay times are illustrated in Figs. 23 and 24.

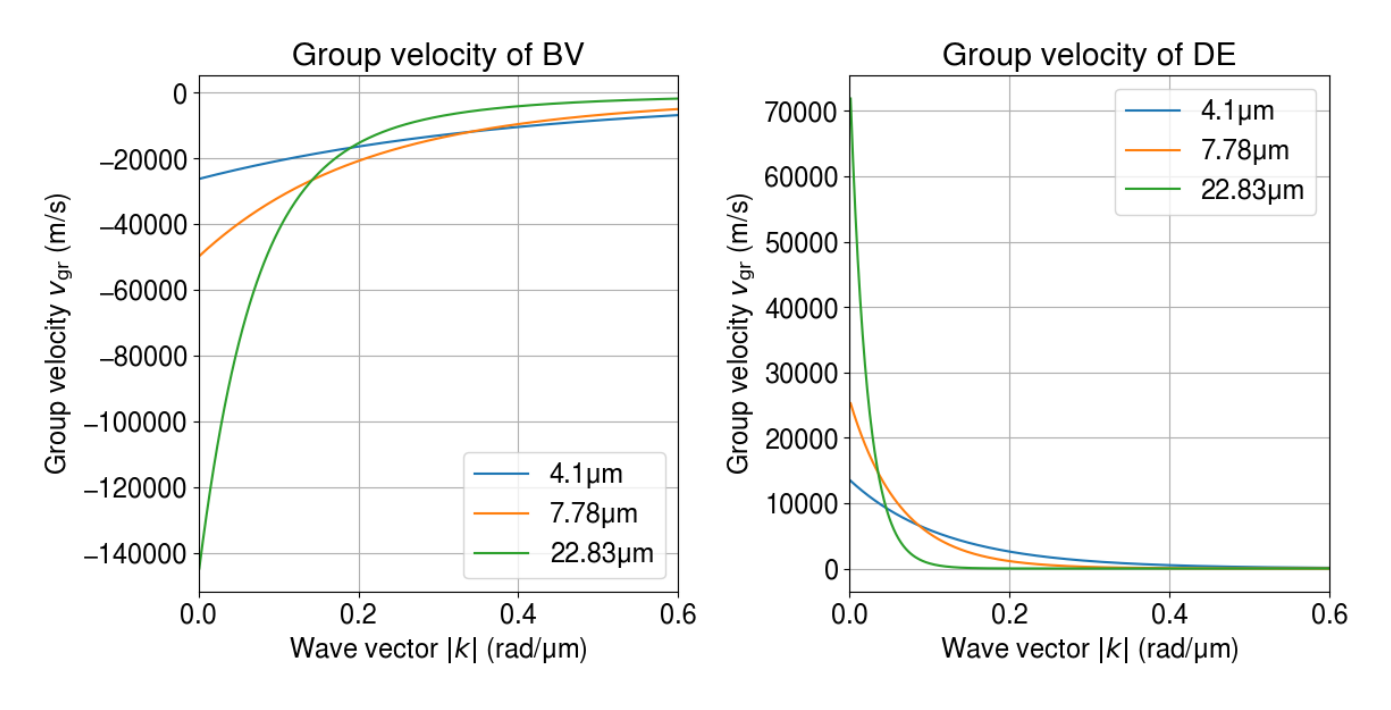


Fig. 21: Theoretical group velocity of YIG at 75mT.

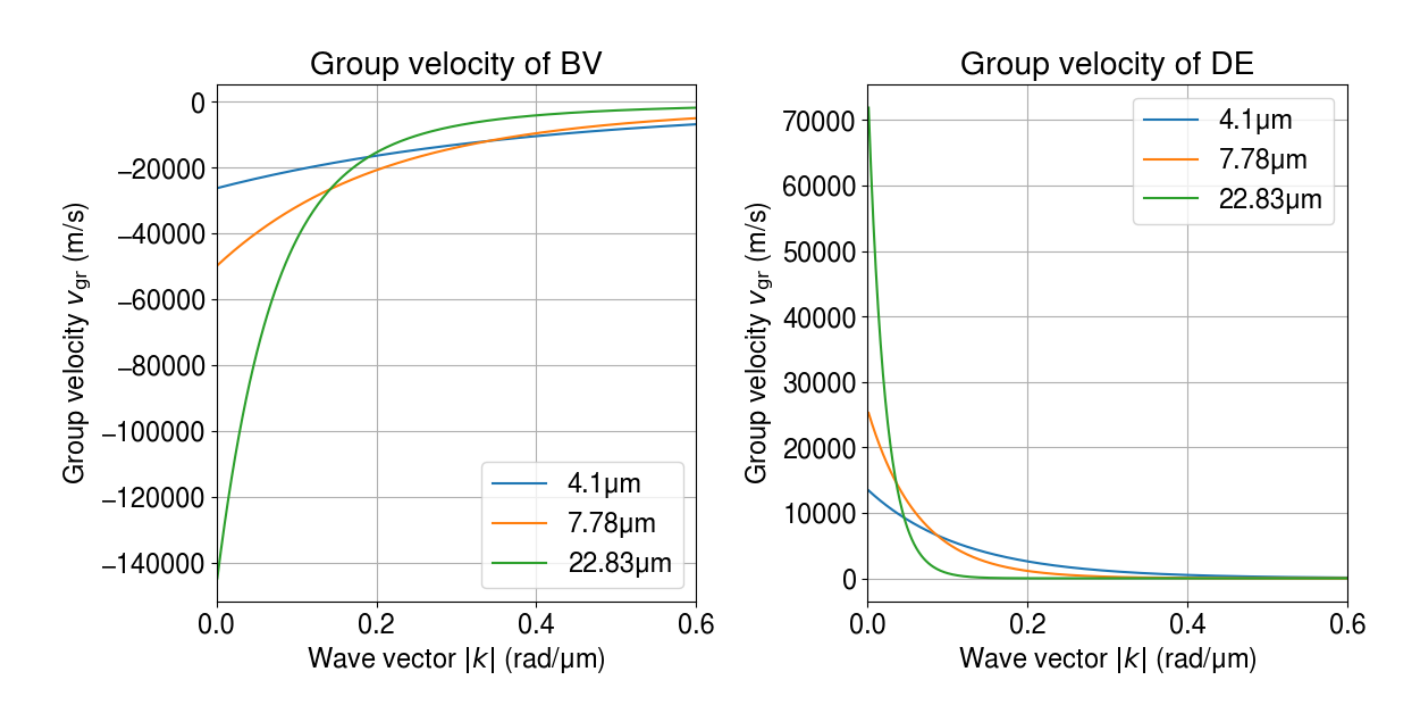


Fig. 22: Theoretical group velocity of YIG at $350 \mathrm{mT}$.

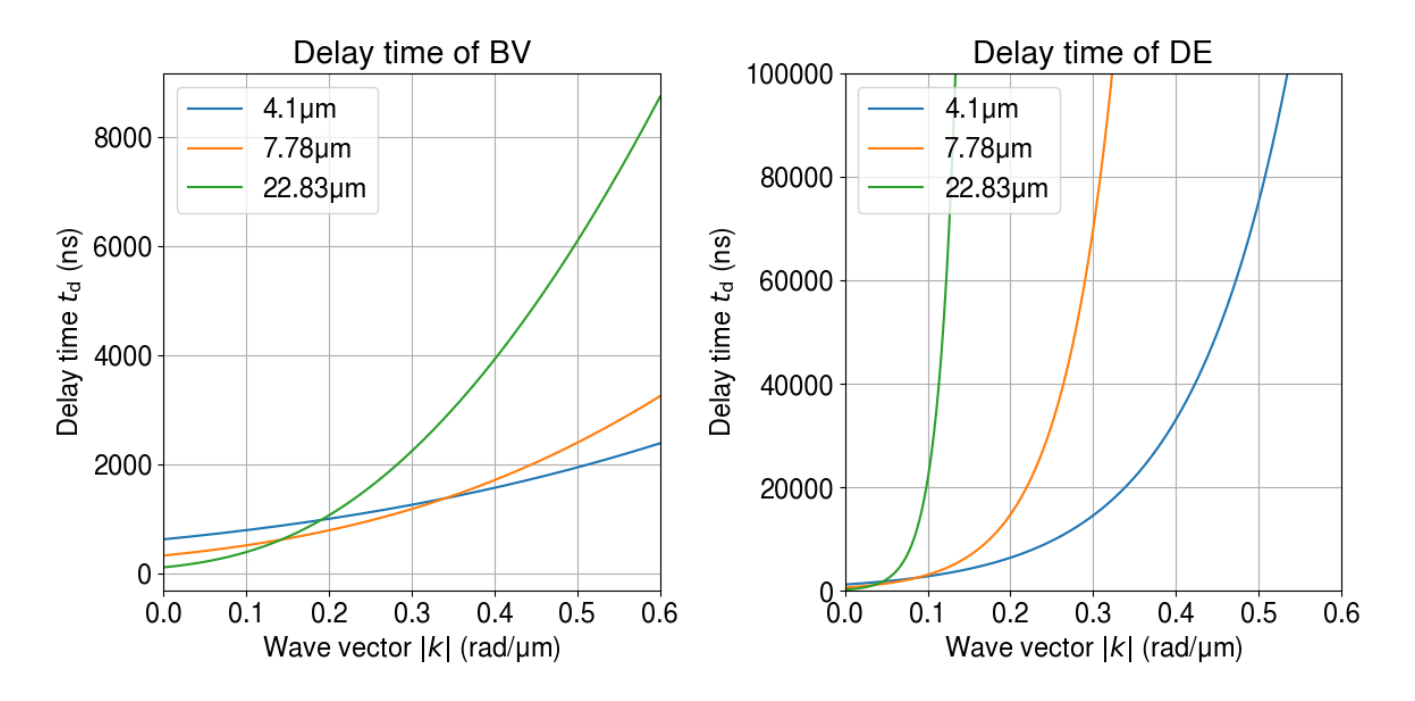


Fig. 23: Theoretical delay of YIG at $75 \mathrm{mT}$.

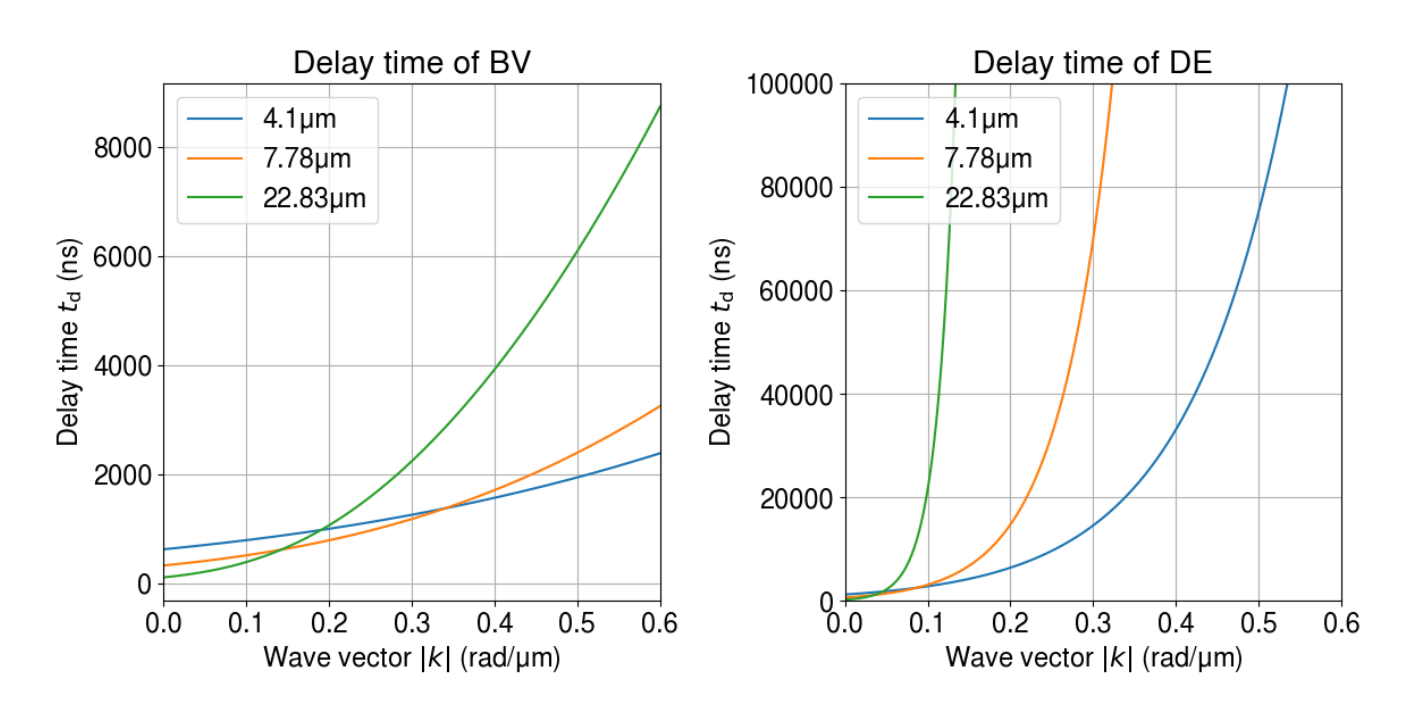


Fig. 24: Theoretical delay of YIG at $350 \mathrm{mT}$.

The theoretical delay time is determined by $t_{\rm d}=\frac{S}{v_{\rm gr}}$, with S being the distance between the two excitation antennas. All theoretically and experimentally determined delay times, as well as the theoretical velocity, are given in Table 2.

configuration	theor. velocity (m/s)	theor. delay (ns)	exp. delay peak (ns)	
4.1µm:				
BV : 75mT	16259	1015 ± 32	638.00 ± 0.10	
BV : 350mT	24356	677 ± 21	493.20 ± 0.10	
DE : 75mT	42132	392 ± 13	306.89 ± 0.10	
DE : 350mT	13524	1220 ± 39	381.00 ± 0.10	
7.78 µ m:				
BV : 75mT	33050	499 ± 16	501.22 ± 0.10	
BV : 350mT	49507	333 ± 11	328.13 ± 0.10	
DE : 78.7mT	77485	212.9 ± 6.9	259.55 ± 0.10	
DE : 350mT	25663	643 ± 21	446.20 ± 0.10	
22.83 µ m:				
BV : 75mT	98026	168.3 ± 5.2	188.67 ± 0.10	
BV : 350mT	146840	112.4 ± 3.5	107.27 ± 0.10	
DE : 78.7mT	234602	70.3 ± 2.3	111.33 ± 0.10	
DE : 350mT	75305	219.1 ± 7.1	165.93 ± 0.10	

Table 2: Measured and theoretical delay times at different magnetic field strengths and magnetisation geometries for YIG.

The uncertainty in the theoretical velocity was derived from the uncertainty in the antenna distance. The delay time for the $7.78\mu m$ -thick sample in the DE configuration under a bias field of 350mT is shown in Fig. 25.

In some measurements, the spectrum exhibits more pronounced complex reflection peaks. An example is presented in Fig. 26, where the SW transmission in DE geometry in a $4.1\mu\text{m}$ -thick sample at a bias field of 75mT is analysed in detail.

Fig. 27a shows the IFFT of the S_{21} signal on a logarithmic scale. Each uniquely colour-coded peak is analysed separately and then merged into the graph. After isolating each peak within its respective time window and zeroing out other signals, the individual peaks were converted back to the frequency domain via FFT and recombined into the S_{21} transmission spectrum (Fig. 27b).

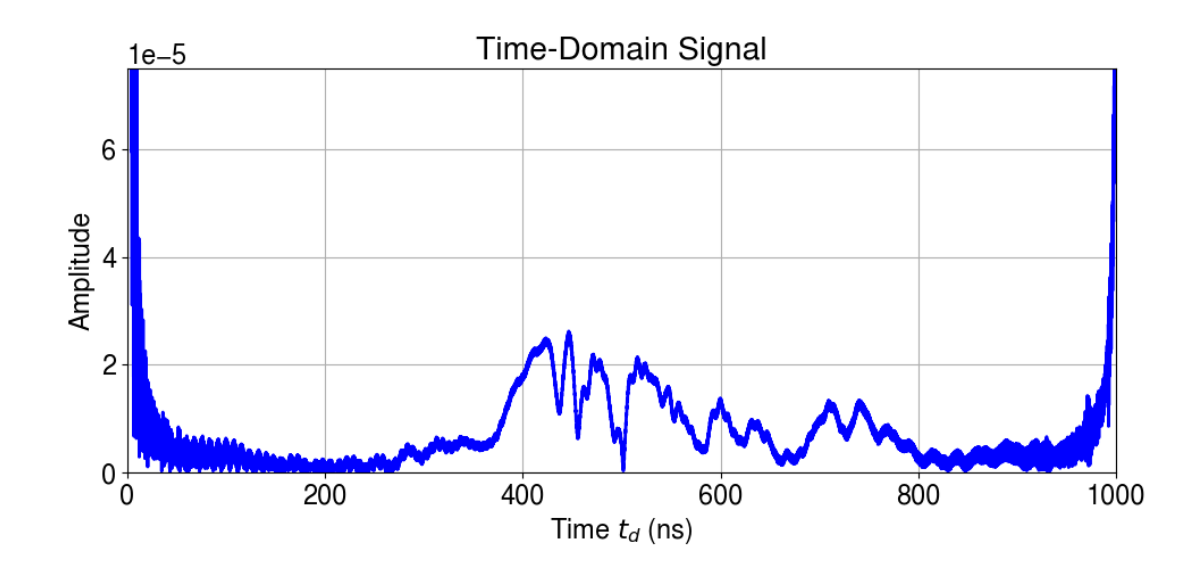


Fig. 25: Delay time of $7.78 \mu \mathrm{m}\text{-thick YIG}$ in the DE configuration and an external field of $350 \mathrm{mT}$

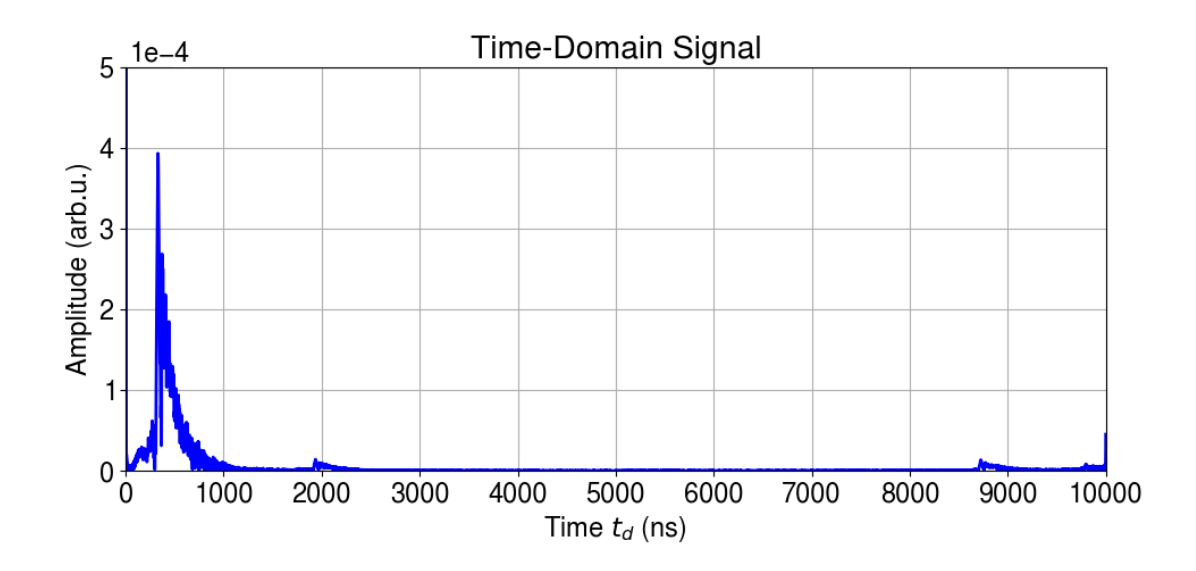


Fig. 26: Delay time of $4.1\mu m$ -thick YIG in the DE configuration and an external field of 75mT, resulting from a IFFT.

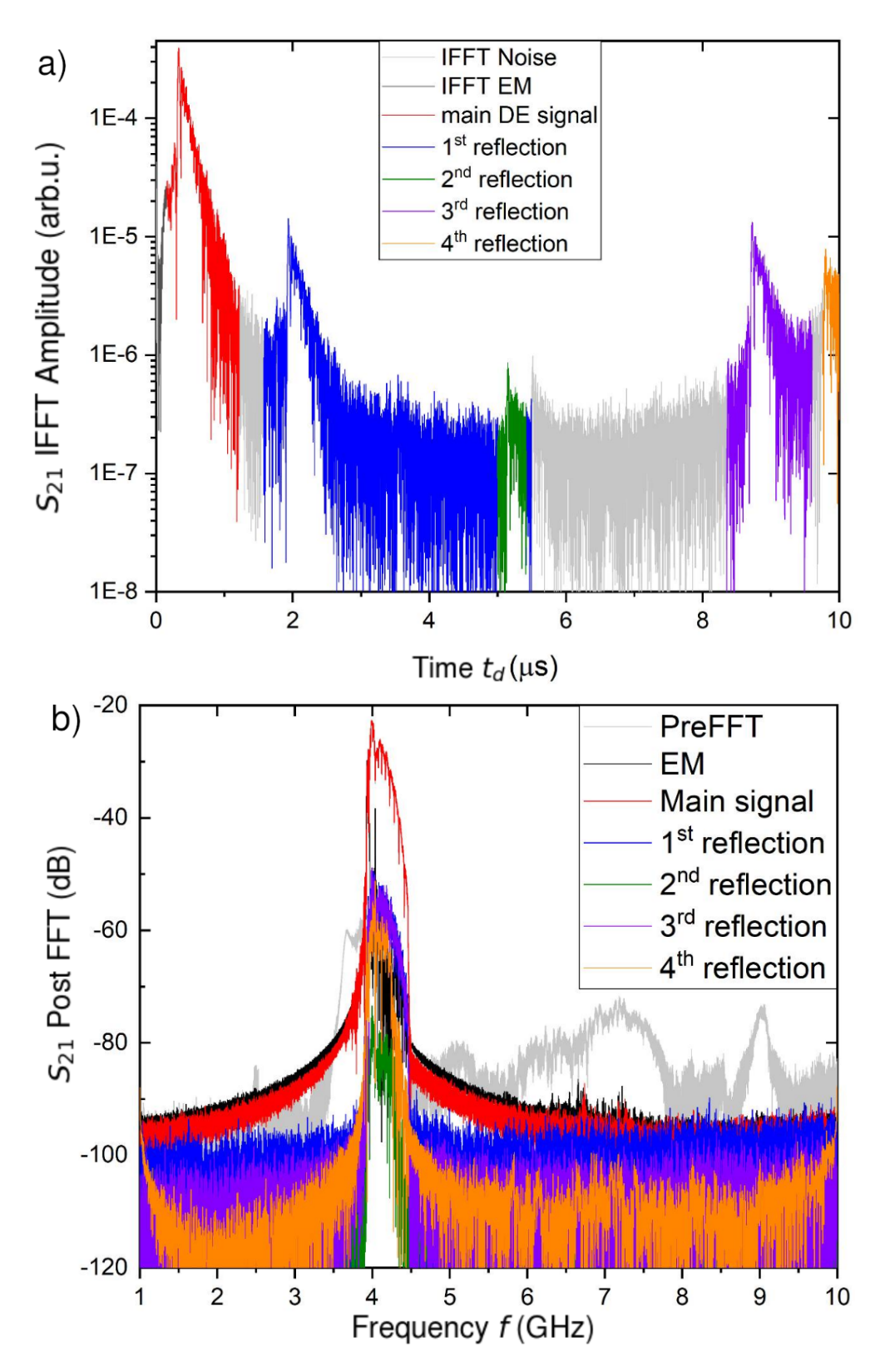


Fig. 27: a) IFFT of the $4.1 \mu m$ -thick YIG sample in the DE geometry under an external field of 75 mT, separated into individual signal contributions. b) S_{21} transmission corresponding to the signals in a), obtained by converting back via FFT.

For comparison, the raw data, background-subtracted data, and FFT-processed

data for a $4.1\mu\text{m}$ -thick YIG film in the DE configuration can be seen in Fig. 28 at 75mT and Fig. 29 at 350mT, showing an even more significant difference. The insertion loss, dynamic range, and bandwidth extracted from the FFT-processed data are shown in Table 3.

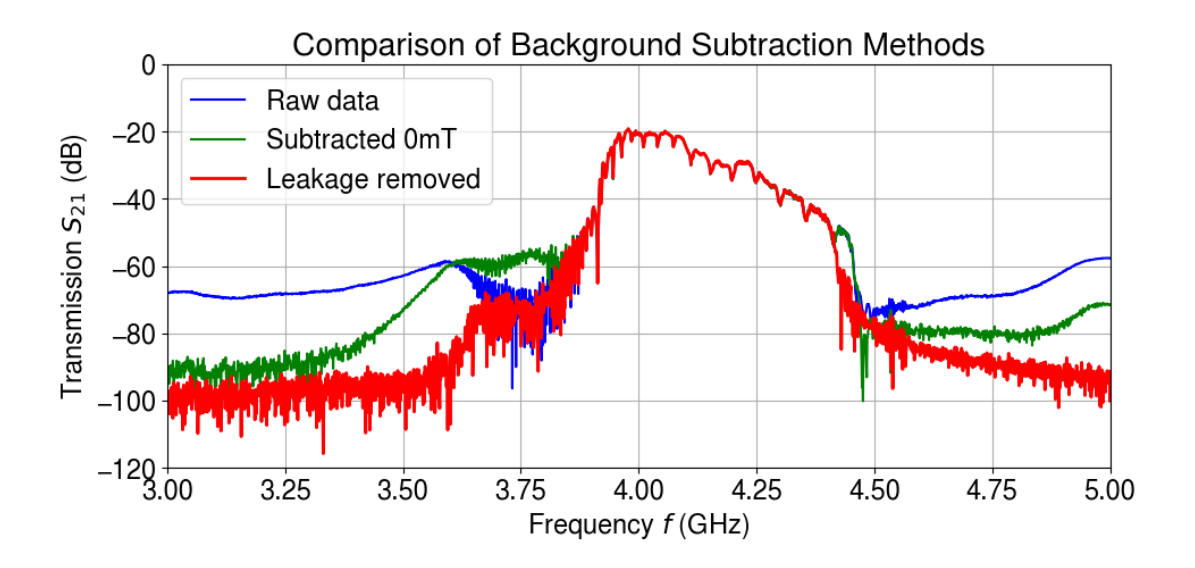


Fig. 28: Comparison of the raw data, background-subtracted data, and FFT-processed data for a $4.1\mu\mathrm{m}$ -thick YIG film in the DE configuration with an external magnetic field of $B_{\mathrm{ext}}=75\mathrm{mT}$.

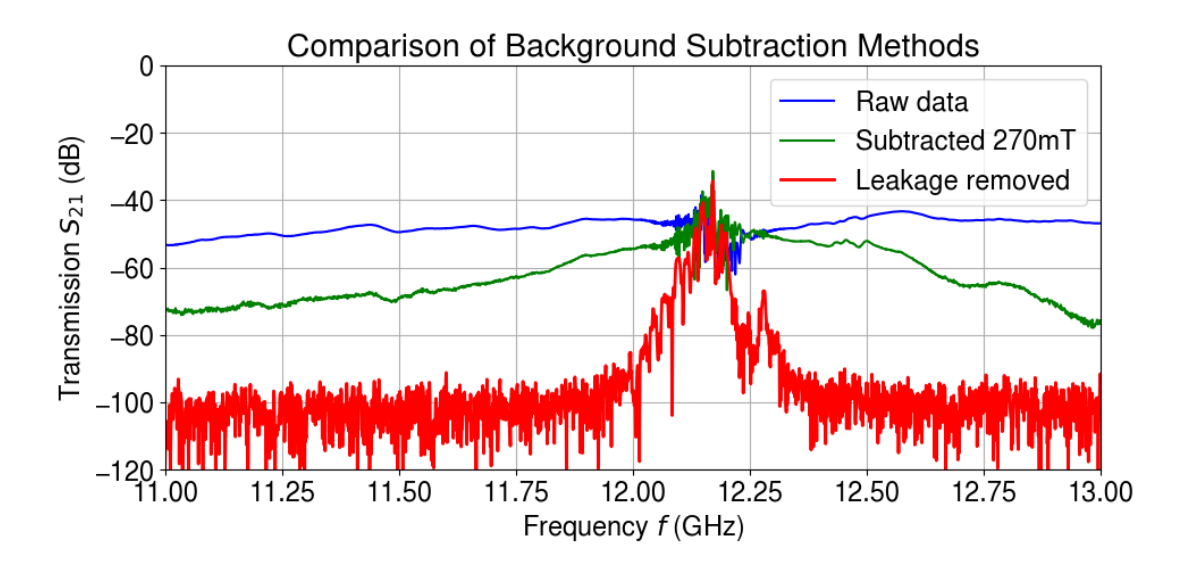


Fig. 29: Comparison of the raw data, background-subtracted data, and FFT-processed data for a $4.1 \mu m$ -thick YIG film in the DE configuration with an external magnetic field of $B_{\rm ext} = 350 {\rm mT}$.

Sample uncertainty:	$\begin{array}{c} \text{insertion loss} \ (dB) \\ \pm 0.10 dB \end{array}$	$\begin{array}{c} \text{dynamic range } (\mathrm{dB}) \\ \pm 5.0 \mathrm{dB} \end{array}$	$\begin{array}{c} \textbf{bandwidth} \ (GHz) \\ \pm 0.01 GHz \end{array}$	
	S_{21}/S_{12}	S_{21}/S_{12}	S_{21}/S_{12}	
4.1 µ m:				
BV : 75mT	-33.28/-32.91	63.5/60.0	0.048/0.021	
BV : 350mT	-31.90/-29.09	63.1/59.8	0.061/0.011	
DE : 75mT	-19.19/-39.58	70.8/74.2	0.138/0.029	
DE : 350mT	-34.42/-56.40	57.5/42.1	0.002/0.005	
7.78µm:				
BV : 75mT	-31.00/-32.42	79.5/62.8	0.018/0.024	
BV : 350mT	-32.12/-30.02	63.1/64.5	0.031/0.056	
DE : 78.7mT	-17.96/-36.29	76.2/51.0	0.109/0.079	
DE : 350mT	-31.63/-49.0	61.6/41.3	0.036/0.006	
22.83µm:				
<i>BV</i> : 75mT	-20.70/-21.37	54.7/49.7	0.095/0.095	
BV : 350mT	-16.49/-17.19	67.5/69.1	0.052/0.070	
DE : 78.7mT	-14.71/-25.32	40.8/41.6	0.228/0.107	
DE : 350mT	-21.39/-33.14	68.0/61.5	0.096/0.015	
Flipped, 75mT	S_{21}	S_{21}	S_{21}	
<i>BV</i> : 4.1µm	-32.52	70.6	0.012	
<i>ΒV</i> : 7.78μm	-34.68	70.6	0.008	
<i>BV</i> : 22.83µm	-19.30	54.0	0.016	

Table 3: Insertion loss, dynamic range, and bandwidth at different thicknesses and modes, analysed from the FFT-processed transmission coefficients S_{21} and S_{12} .

The lowest insertion loss of $(-14.71 \pm 0.10) dB$ corresponds, via the relation $P_{dB} = 10 \cdot \log_{10} P$, to a power loss of $(96.619 \pm 0.078)\%$.

A visual comparison of the transmission signals for the $7.78\mu\mathrm{m}$ -thick YIG film in the DE configuration is shown in Fig. 30, while Fig. 31 presents the transmission for the $22.83\mu\mathrm{m}$ -thick film in the BVMSW configuration. Fig. 32 illustrates the measured difference between the two measured sides for the $4.1\mu\mathrm{m}$ -thick YIG film in the BVMSW configuration, and Fig. 33 compares the transmission for films of different thicknesses.

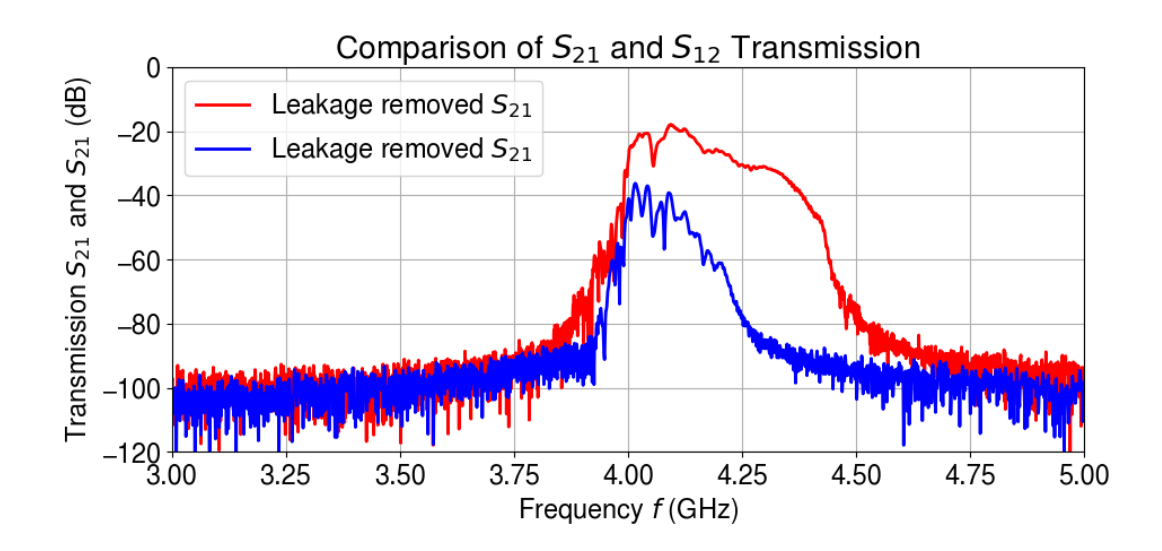


Fig. 30: Comparison of the S_{12} and S_{21} transmission for a $7.78\mu\mathrm{m}$ -thick YIG film in DE configuration with an applied external field of $B_{\mathrm{ext}}=78.7\mathrm{mT}$.

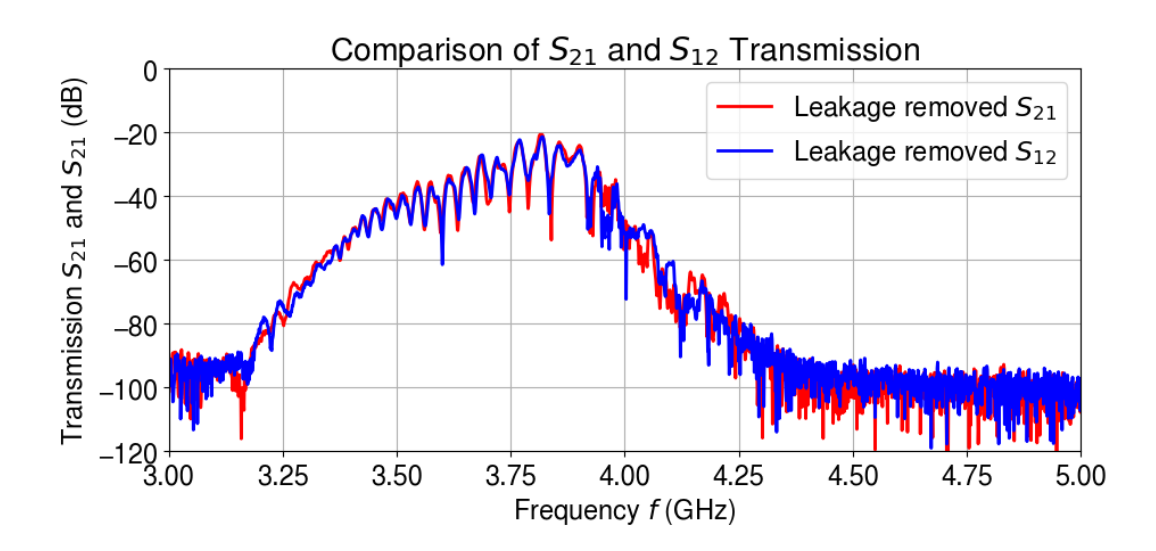


Fig. 31: Comparison of the S_{12} and S_{21} transmission for a $22.83\mu\mathrm{m}$ -thick YIG film in BVMSW configuration with an applied external field of $B_{\mathrm{ext}}=75\mathrm{mT}$.

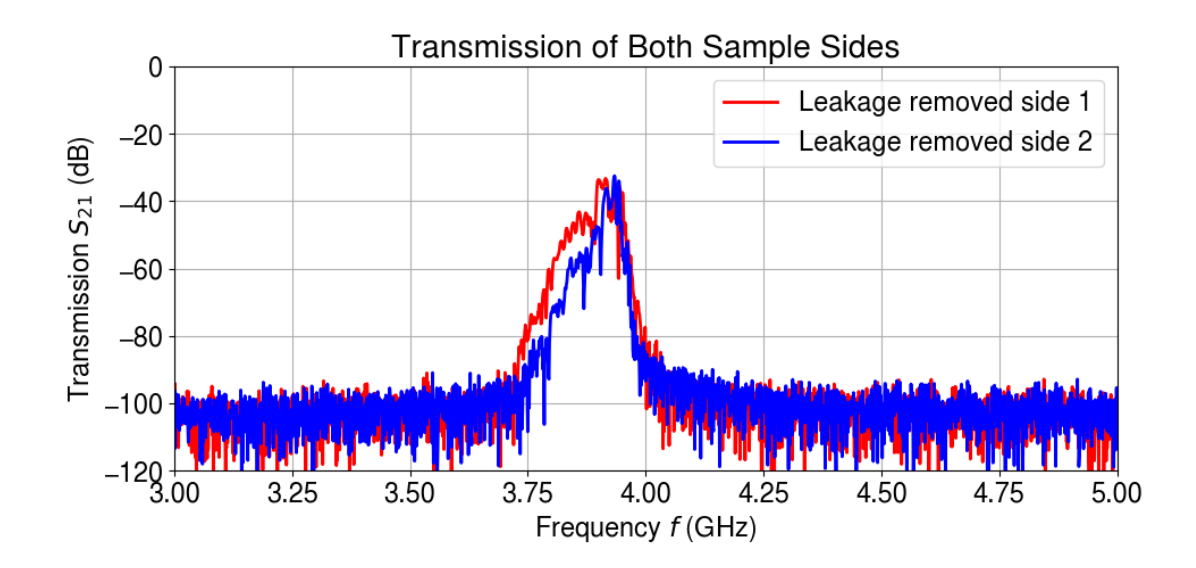


Fig. 32: Difference in transmission for a $4.1\mu\mathrm{m}$ -thick YIG film in BVMSW configuration with an applied external field of $B_{\mathrm{ext}} = 75\mathrm{mT}$, when the sample is flipped.

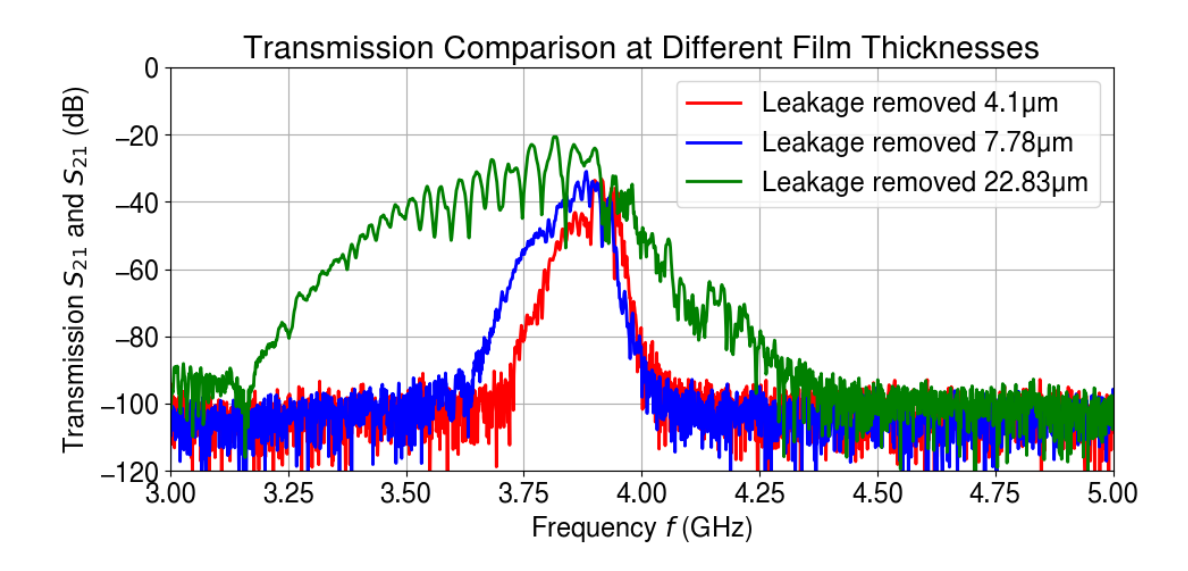


Fig. 33: Comparison of transmission for $4.1\mu\mathrm{m}$, $7.78\mu\mathrm{m}$, and $22.83\mu\mathrm{m}$ -thick YIG films in BVMSW configuration with an external magnetic field of $B_{\mathrm{ext}} = 75\mathrm{mT}$.

6 Discussion

6.1 Raw data

The measurements show distinctive excitations for every applied magnetic field strength, as illustrated in Figs. 12–15. As expected from theory, increasing the magnetic field results in a corresponding increase in excitation frequency.

In PSWS spectroscopy, the measured signal generally contains not only the magnetic response of the sample, but also a substantial microwave background. This background originates from the experimental setup and includes direct electromagnetic contribution, frequency-dependent transmission and reflection of cables, adapters and connectors, as well as standing-wave patterns arising from impedance mismatches. Additional contributions may stem from instrumental artifacts. To isolate the magnetic response from a sample, it is therefore necessary to subtract a suitable reference signal, effectively removing the frequency-dependent microwave background.

Subtracting reference transmission signals at $0 \mathrm{mT}$ and $270 \mathrm{mT}$ reduced the overall noise level, but the spectra still contained considerable non-spin-wave contributions. These became more pronounced at higher frequencies, where the applied field differed by several hundred mT from the reference. Improved results may be obtained by applying reference subtraction within narrower frequency windows and using multiple such segments to span the full frequency range.

6.2 FMR

Since the experiment was designed for PSWS rather than FMR spectroscopy, the FMR was determined by extracting the beginning of the signal (lowest frequency at which excitation occurs) for the DE configuration, and the end of the signal (highest frequency of excitation) for the BV configuration. To avoid subjectivity in defining the signal onset and cutoff, the edges of the SW transmission spectra were extracted — from the low-frequency side for the DE geometry and from the high-frequency side for the BV geometry. Because the strongest excitation for

both spin waves and the antenna occurs at the FMR, these two quantities are expected to correlate closely. As illustrated in Fig. 16, this approach yielded a strong correlation between the experimental data and the theoretical predictions from the Kittel formula. Data from Table 4 demonstrate that, for both DE and BV modes, the frequency of strongest excitation can be accurately predicted by the Kittel formula, with the applied external magnetic field being the only significant parameter — independent of the in-plane magnetic configuration or film thickness. It should be noted that the FMR of samples with otherwise similar parameters may vary slightly depending on the growth conditions and fabrication methodology. Overall, the results confirm that dipolar interactions dominate at the microscale, whereas the contribution of exchange interactions is negligible.

6.3 Dispersion relation

The theoretical dispersion relation was calculated and shows a more rapid increase in frequency range for thicker samples. The spin wave (SW) dispersion spectra determine the magnetisation geometry. Especially notable is the monotonic increase in frequency with the wave vector for DE, giving it its positive and steeply sloped dispersion relation, and therefore a high group velocity $|v_{\rm gr}|$. In contrast, the dispersion relation of BV exhibits a known negative slope, which remains comparatively shallow (see Fig. 17), resulting in a slower $|v_{\rm gr}|$. The higher group velocity of DE increases the propagation length and, as a result, improves its transmission efficiency. Additionally, irrespective of thickness or magnetic configuration (BV or DE), the FMR frequency remains constant, in agreement with the Kittel formula.

Furthermore, the theoretical analysis correlates well with the measured transition frequency profiles when the antenna excitation efficiency is taken into account, as shown in Figs. 18 and 19. However, as briefly noted in the Results section, an adjustment of the theoretical magnetic field was necessary to achieve good overlap between the experimental data and the theoretical dispersion relations. Since the magnetic field is measured near the sample, some error arises due to the distance between the Hall sensor and the probe, as well as the field's inhomo-

geneity. At the time of writing this thesis, improvements to the Hall sensor holder are underway (see Chapter 3), which will enable testing of the sensor placement's impact in the near future.

6.4 Time gating

The transmission signal was successfully transformed into its delay time, allowing unwanted signals to be filtered out—most notably the excitation caused by EMwave leakage, which accounts for the large excitation spike at lower delay times due to its high velocity. As illustrated in Fig. 20, this method achieves effective isolation of the SW excitation signal.

Leakage removal via IFFT and FFT consistently improved the signal compared the raw data and the background-subtracted data, as shown, for example, in Fig. 28. In the case of the measurement on a $4.1 \mu m$ -thick YIG film in the DE configuration with an external field of 350 mT, the signal-to-noise ratio was improved to a state reliable for further analysis dynamic range and bandwidth, as pictured in Fig. 29.

6.5 Group velocity and delay time

As expected, the theoretical calculations, illustrated in Fig. 21 and Fig. 22, show a negative group velocity $v_{\rm gr}$ for BV, but a positive $v_{\rm gr}$ for DE. It stands out that the absolute value of the group velocity, $|v_{\rm gr}|$, is always greatest in the vicinity of the FMR, independently of thickness, magnetic configuration, or applied field. Furthermore, the thickness-dependent Kalinikos–Slavin dispersion shows monotonic growth with d at a fixed in-plane wave vector k. Hence, the slope of the dispersion relation increases with the thickness of the sample, consequently resulting in an increased group velocity. Accordingly, the $22.83~\mu \text{m}$ -thick sample possesses the highest theoretical group velocities $|v_{\rm gr}|$, reaching the order of $10^5~\frac{\text{m}}{\text{s}}$, as shown in Tab. 2. Since the delay time is inversely proportional to the group velocity, the reverse is observed for the expected delay time: a higher delay time is shown in Fig. 23 and Fig. 24 for thinner samples near the FMR.

The measured delay time near the FMR agrees well with the theoretical predic-

tions for the $7.78~\mu m$ and $22.83~\mu m$ thick samples, with the error being under 55~ns in all cases, except for the $7.78~\mu m$ thick YIG in the DE configuration at an applied field strength of 350~mT. This deviation is likely caused by the measurement error due to field uncertainty at sample's position, although the theoretical value still falls within the measured delay window, as shown in Fig. 25. The high pick at the right edge of IFFT time scale at Fig. 25 corresponds, most probably, to the accumulation of signals arriving after $1~\mu s$.

The measurements for the $4.1~\mu m$ -thick sample show significant shows a complex spin-wave spectra due to a combination of non-reciprocal measurement configuration and sample's geometry (small cracks on a side). Notably, the theoretical analysis predicts a delay time exceeding 1000~ns for this sample. Consequently, a remeasurement was performed using a reduced frequency step of 100~kHz instead of the previous 1~MHz, resulting in a calculated delay time of up to 10,000~ns. This allowed for the successful extraction of SW reflections, as shown in Fig. 27. Multiple complex reflections of the main signal from the sample's edges, cracks and from antennas are visible in the logarithmic scale of the IFFT time spectrum, which correspond to decreased transmission signals at the same excitation frequency as the main DE SW signal. However, the experimentally observed delay time peaks for the $4.1~\mu m$ -thick sample still exhibit significant deviations from the theoretically expected delay times. The analysis of such complex data is beyond the scope of this work but could be addressed in future research, for example, as part of a master's thesis project.

Since group velocity of DE increases with the thickness of the film d, the $22.83\mu m$ -thick sample show the lowest delay time, of the measured samples, for a fixed propagation distance, field and in-plane wave vector k.

6.6 Insertion loss, dynamic range, bandwidth

The high group velocity of DE results in longer propagation length. In addition, the close proximity of the surface modes and the microstrip antennas provides a strong bias field within the bulk of the spin wave, ensuring higher excitation and detection efficiency for DE compared to BV. As shown in Table 3, when the thick-

ness of the sample and the applied field are equal, the DE configuration consistently exhibits lower losses than the BV configuration. This makes DE especially appealing for experimental research and device applications, particularly when combined with a low Gilbert damping material such as YIG. Moreover, the most significant difference between DE and BV lies in the asymmetry between the transmission signals S_{21} and S_{12} . Whereas BV shows only minor differences between the two signals (see Fig. 31), DE exhibits a loss of at least $10\,\mathrm{dB}$ more in S_{12} compared to S_{21} , as illustrated in Fig. 30. Since DE spin waves are non-reciprocal, a microstrip antenna placed on top of a film excites DE waves more strongly in one direction than in the other (see Section 2.2.2). This contrasts with BV waves, where reciprocal propagation leads to port-independent excitation [8].

In addition, as discussed in the previous section, thicker samples have higher group velocities, thus lower delay times, leading to reduced dissipation for a given lifetime τ . Therefore, thicker samples result in lower insertion loss, as shown in Fig. 33. Unsurprisingly, the best transmission was achieved with the $22.83\,\mu\mathrm{m}$ -thick sample in the DE configuration, with an insertion loss of $(-14.71\pm0.10)\,\mathrm{dB}$, which still corresponds to a $(96.619\pm0.078)\%$ transmission loss. No pattern was observed regarding the influence of the external field, due to the many variables it affects — including shifts in frequency (which in turn reduce the lifetime, as described by the viscous Gilbert damping), as well as changes in dispersion relation, hence the group velocity and delay time respectfully.

The measured samples have YIG grown on both sides, eliminating the possibility of using the wrong side during measurements. Transmission measurements on the flipped sample side showed only minor differences of approximately $2~\mathrm{dB}$ in insertion loss, as summarized in Table 3, and exhibited a similar signal profile, as illustrated in Fig. 32. The small observed differences between the two sample sides are therefore attributed to minor measurement uncertainties, such as slight variations in thickness and imperfect sample placement.

The dynamic range of the signals once again demonstrates the effectiveness of leakage removal via IFFT. However, strong fluctuations in the noise required assigning a relatively large uncertainty to the dynamic range. Even with this consid-

eration, reliable extraction of the excitation signal is ensured—an important factor for potential applications such as frequency filters. Nevertheless, time-gating itself is not practical outside experimental analysis; therefore, alternative improvements like enhanced antenna designs will be necessary for future devices [16]. In most cases, the bandwidth did not exceed $100 \mathrm{MHz}$, with the exception of the DE configuration at around $75 \mathrm{mT}$. This limited bandwidth results from the definition of the half-power point, set at $-3 \mathrm{\,dB}$ below the insertion loss.

7 Conclusion and Outlook

The goal of measuring and analysing propagating SW in YIG films at varying macroscale thicknesses has been a success. The excitations measured with the VNA exhibit peaks that agree with the theoretically computed FMR derived from the Kittel equation (see Fig. 16). Therefore, it was also possible to assign the experimentally extracted transmission signals to their corresponding dispersion relations. However, this was only achieved with slight adjustments to the theoretical magnetic field. A more accurate measurement of the magnetic field will soon be realised, due to an improved holder setup for the Hall sensor, in the design of which I personally contributed. This will make it possible to verify in future experiments whether the deviations were caused by inaccurate measurements.

Thanks to the use of an IFFT, it was possible to extract the delay time for each signal, revealing the expected correlation with the spin waves' group velocity. Only the $4.1 \mu \mathrm{m}$ -thick YIG sample exhibited unexpected deviations from the theoretical analysis, which could not be fully resolved within the scope of this thesis. Nevertheless, the expected reflections of the excitation signal were successfully observed.

In addition, the FFT allowed for the extraction of an improved signal, most notably by removing the excitations whose delay times correspond to those produced by EM waves. This resulted in a high dynamic range of the transmission signal, which is an important factor for potential use cases such as high-frequency filters. However, further improvements in insertion loss are needed, as even the most efficient measured transmission — a 22.83µm-thick YIG sample in the DE configuration (see Fig. 3) — exhibited losses too high for industrial use. Improved efficiency could possibly be achieved by using differently shaped excitation antennas.

References

- [1] K. O. Levchenko, K. Davídková, J. Mikkelsen, and A. V. Chumak, "Review on spin-wave RF applications," 2025. Corresponding authors: *khrystyna.levchenko@univie.ac.at, †andrii.chumak@univie.ac.at.
- [2] A. G. Gurevich and G. A. Melkov, *Magnetization Oscillations and Waves*. Boca Raton: CRC Press, 1996.
- [3] A. V. Chumak, "Fundamentals of magnon-based computing," *arXiv preprint arXiv:1901.08934*, 2019.
- [4] D. D. Stancil and A. Prabhakar, *Spin Waves: Theory and Applications*. New York: Springer, 1 ed., 2009.
- [5] K. M. Krishnan, *Fundamentals and Applications of Magnetic Materials*. Oxford: Oxford University Press, 2016.
- [6] B. Heinz, "Herstellung und untersuchung der magnetisierungsdynamik in einzelnen yttrium-eisen-granat mikrostrukturen," diplomarbeit in experimentalphysik, Technische Universität Kaiserslautern, Fachbereich Physik, Nov. 2016.
- [7] Tektronix, Inc., "What is a vector network analyzer and how does it work?," n.d. Accessed: 2025-05-12.
- [8] A. A. Serga, A. V. Chumak, and B. Hillebrands, "Yig magnonics," *Journal of Physics D: Applied Physics*, vol. 43, 2010.
- [9] J. Coey, *Spin Waves: Theory and Applications*. Cambridge: Cambridge University Press, 2009.
- [10] S. Fiorentini, Computation of Torques in Magnetic Tunnel Junctions. Phd thesis, Technische Universität Wien, Fakultät für Elektrotechnik und Informationstechnik, Wien, Juli 2023. Dissertation zur Erlangung des akademischen Grades eines Doktors der technischen Wissenschaften. Betreuung: PD MSc PhD Viktor Sverdlov, O.Univ.Prof. Dipl.-Ing. Dr.techn. Dr.h.c. Siegfried Selberherr. Matrikelnummer: 11839446.

- [11] L. Flajšman, Magneto-Optical Study of the Dynamic Properties of Magnetic Nanostructures and Nanostructured Metamaterials. Doctoral thesis, Brno University of Technology, Central European Institute of Technology (CEITEC), Brno, Czech Republic, 2019. Also published in Czech as: Studium dynamických vlastností magnetických nanostruktur a nanostrukturovaných metamateriálů pomocí magneto-optických metod.
- [12] L. Exl, D. Suess, and T. Schrefl, "Introduction to microscopy," 2023. Accessed: 2025-08-27.
- [13] S. D. Joseph and E. Ball, "Series-fed millimeter-wave antenna array based on microstrip line structure," *IEEE Open Journal of Antennas and Propagation*, vol. PP, pp. 1–1, 2023.
- [14] D. M. Pozar, *Microwave Engineering*. Hoboken, NJ: Wiley, 4th ed., 2012.
- [15] V. Cherepanov, I. Kolokolov, and V. L'vov, "The saga of yig: Spectra, thermodynamics, interaction and relaxation of magnons in a complex magnet," North-Holland, unknown. Department of Physics, University of Manitoba; Institute of Nuclear Physics, Novosibirsk; Weizmann Institute of Science.
- [16] K. O. Levchenko, K. Davídková, R. O. Serha, M. Moalic, A. A. Voronov, C. Dubs, O. Surzhenko, M. Lindner, J. Panda, Q. Wang, O. Wojewoda, B. Heinz, M. Urbánek, M. Krawczyk, and A. V. Chumak, "1D YIG hole-based magnonic nanocrystal (SUPPLEMENTARY MATERIALS)." Unpublished supplementary material, 2025. Affiliations: University of Vienna, Adam Mickiewicz University, INNOVENT e.V., CEITEC BUT, HUST, RPTU Kaiserslautern.

Appendix

field	BV:	(GHz)	±0.06	DE:	(GHz)	±0.06	theor.
$\pm 2 \cdot 10^{-4}$	$4.1 \mu \mathrm{m}$	$7.78 \mu\mathrm{m}$	$22.83 \mu \mathrm{m}$	4.1 µ m	$7.78 \mu\mathrm{m}$	$22.83 \mu \mathrm{m}$	
25mT	2.067	2.026	2.024	2.034	2.059	2.197	1.984
50mT	3.074	2.888	2.861	3.044	3.01	3.018	2.976
75mT	3.915	3.838	3.819	3.978	3.992	4.184	3.841
100mT	4.729	4.648	4.625	4.816	4.787	4.944	4.651
125mT	5.539	5.441	5.41	5.564	5.583	5.693	5.431
150mT	6.29	6.18	6.166	6.333	6.325	6.309	6.191
175mT	7.026	6.988	6.919	7.092	7.066	7.028	6.939
200mT	7.824	7.795	7.753	7.836	7.818	7.748	7.678
225mT	8.551	8.502	8.49	8.578	8.546	8.635	8.410
250mT	9.284	9.233	9.212	9.331	9.29	9.356	9.137
275mT	9.966	9.969	9.932	9.996	9.989	10	9.860
300mT	10.693	10.694	10.652	10.726	10.72	10.675	10.580
325mT	11.416	11.388	11.372	11.449	11.392	11.44	11.298
350mT	12.138	12.112	12.126	12.171	12.114	12.118	12.013
375mT	12.874	12.829	12.844	12.89	12.832	12.774	12.727
400mT	13.592	13.551	13.544	13.609	13.549	13.554	13.439
425mT	14.308	14.267	14.237	14.311	14.256	14.207	14.150
450mT	15.023	14.999	14.949	15.026	14.977	14.987	14.860
475mT	15.739	15.692	15.665	15.742	15.69	15.598	15.569
500mT	16.45	16.426	16.374	16.455	16.396	16.308	16.278
525mT	17.165	17.137	17.079	17.165	1	17.041	16.985
550mT	17.875	17.849	17.789	17.875	17.84	17.78	17.692
575mT	18.6	18.583	18.496	18.586	18.554	18.491	18.399
600mT	19.31	19.29	19.204	19.294	19.258	19.202	19.105
625mT	/	19.953	19.913	20.002	19.967	19.902	19.810
650mT	20.815	20.708	20.503	20.697	20.677	20.619	20.516
675mT	21.478	21.415	21.41	21.422	/	21.283	21.221
700mT	22.178	22.122	21.925	22.154	22.079	21.995	21.925
725mT	22.721	22.881	22.809	22.821	22.792	22.694	22.629
750mT	23.401	23.479	23.305	23.535	23.488	23.444	23.333
775mT	24.159	24.238	24.23	24.246	24.208	24.153	24.037
800mT	24.856	24.942	24.668	24.951	24.901	24.861	24.741

Table 4: Measured FMR at different magnetic field strengths, different thickness of YIG film and the magnetisation geometries compared to theoretical Kittel formula.